On the Tidal Currents Observed by Moorings in Prydz Bay, East Antarctica

Chengyan Liu[1,2], Zhaomin Wang[1*,2], Robin Robertson[3], Chen Cheng[4,2], Xi Liang[5], Yang Wu[1,2], Xiang Li[6], Yu Liu[7], and Xiaojun Yuan[8]

[1]*International Polar Environment Research Laboratory, College of Oceanography, Hohai University, No1, Xikang Road, 210098, Nanjing, China.*

[2]*Southern Marine Science and Engineering Guangdong Laboratory (Zhuhai), China.*

[3]*China-ASEAN College of Marine Sciences, Xiamen University, Sepang, Selangor, Malaysia*

[4]*School of Marine Sciences, Nanjing University of Information Science & Technology, Nanjing, China.*

[5]*Key Laboratory of Research on Marine Hazards Forecasting, National Marine Environmental Forecasting Center, Beijing, China.*

[6]*Key Laboratory of Ocean Circulation and Waves, Institute of Oceanology, Chinese Academy of Sciences, China.*

[7]*Marine Science and Technology College, Zhejiang Ocean University, Zhoushan, China.*

[8]*Lamont-Doherty Earth Observatory, Columbia University, Palisades, New York, USA.*

Corresponding author: Zhaomin Wang (zhaomin.wang@hhu.edu.cn)

Abstract

Mooring observations of tidal currents in Prydz Bay, East Antarctica are presented here. They were found to be mixed diurnal-semidiurnal over the continental shelf, with significant seasonality. Barotropic tides dominated the tidal currents at the calving front of the inner continental shelf of the Amery Ice Shelf (AIS), except at the western corner of the AIS where the seabed is abruptly deeper. The spatial and temporal averaged magnitude of tidal currents for all the current meter records was only 2.58 cm s^{-1}, much weaker than in the Ross or Weddell seas. However, the observed maximum tidal current was about 13.12 cm s^{-1} at the AIS calving front. In addition, the ratio of the tidal heat flux standard deviation to the residual heat flux standard deviation could be up to 41% at the AIS front, implying the tides have the potential to modulate the heat content of the AIS cavity. To identify the footprints of the tidal influences on the AIS basal mass balance, we further assessed the temperature and salinity records from six boreholes drilled through the AIS. Interestingly, tide-like pulsing was identified in the ocean layer adjacent to the AIS basal surface, highlighting the potential tidal influences on the heat exchanges at the ice-ocean interface. Our assessment of the tidal currents in Prydz Bay underlines that the critical role of tides should be highlighted in investigations of interactions between the ocean and the AIS, and other ice shelves.

Plain Language Summary

We report on mooring observations of tidal currents in Prydz Bay, East Antarctica. Tides in Prydz Bay are mixed diurnal-semidiurnal and much weaker than that in the Ross Sea and the Weddell Sea, with the averaged magnitude of 2.58 cm s-1 over the continental shelf. The major axes of the tidal ellipses are generally aligned south-north, probably controlled by the topography. The tidal phases are modulated by both the baroclinic and barotropic tidal components. The averaged tidal kinetic energy is not remarkable respect to the total kinetic energy at the Amery Ice Shelf calving front during the observing period. The long-term average tidal heat flux across the Amery Ice Shelf calving front is negligible. However, the changes in the tidal heat flux are nearly half of the changes in the residual heat flux. We also report on borehole observations of tide-like pulsing of potential temperature and salinity, indicating the indispensable tidal influences in the ice-ocean boundary layer. These mooring and borehole data support that the tidal processes should be highlighted in the investigations of the interaction between the Amery Ice Shelf and ocean.

Key Points:

- We assessed the tidal currents in Prydz Bay from observational data from 10 moorings.
- The characteristics of tidal currents and the potential contribution to the ocean heat content were quantitatively documented.
- The hydrographic observations from borehole sites confirmed the important role of tides to the Amery Ice Shelf basal mass balance.

1 Introduction

The tides play a key role in the circulation and hydrographic properties in Antarctic waters through several mechanisms. First, they can favor the exchanges of water masses across the continental shelf break. Second, tidal interactions with topography can generate internal tides. Third, tidal oscillations can result in high-frequency fluctuations of sea ice motion and deformations. At the continental shelf break, tides can bring Circumpolar Deep Water (CDW) onto the continental shelves (Castagno et al., 2017) and enhance the spread and descent of dense Shelf Water (SW) over the continental slope (Ou et al., 2009; Wang et al., 2013). The internal tidal fields generated by the topographic dynamic effects on the barotropic tides can induce mixing, which is particularly important at the continental shelf break where several water masses, including CDW, Ice Shelf Water (ISW), and SW meet. For example, the Antarctic Bottom Water (AABW) formation in the southern Weddell Sea can be enhanced by mixing warm CDW and SW (Robertson et al., 1998; Robertson, 2001). AABW production and exportation are also favored by tidal mixing of Antarctic Surface Water, CDW, and SW at the outer edge of the continental shelf (Padman et al., 2009; Wang et al., 2010; Whitworth & Orsi, 2006) where the simulated maximal tidal currents can exceed 1 m s^{-1} (Padman et al., 2003). The divergence of the tidal currents causes lead formation in the sea ice, enabling higher heat loss from the ocean to the atmosphere and increasing sea ice and dense water production (Koentopp et al., 2005). The convergence of the tidal

ellipses results in rafting and ridging of the sea ice, which decreases sea ice formation. In the inner continental shelf, tidal processes can modify the characteristics of water masses (Padman et al., 2009) and oceanic mean circulation (Robertson et al., 1998) before they flow in the sub-ice-shelf cavity. Consequently, tides can modulate the ice shelf basal melting and alter the thermohaline circulation in the sub-ice-shelf cavity (Padman et al., 2003). At the Pine Island Bay Ice Shelf front, tides can pump water into the sub-ice-shelf cavity (Robertson, 2016). Under the ice shelves, tidal currents can enhance the turbulence by providing friction through ice-water drag (Hellmer & Olbers, 1989; Holland & Jenkins, 1999) and influence ice shelf melting (Robertson, 2013; Jendersie et al., 2018). Additionally, differences in tidal elevations also rhythmically stress the ice shelves on a daily basis, weakening their structure (Hulbe et al., 2016).

In the past decades, most tidal measurements around Antarctica were focused on the vertical tide signal, i.e., tide elevations. Tidal observations were provided by both in situ and remote instruments, including tide gauges, tiltmeters, and satellite altimeter measurements. Lutjeharms et al (1985) documented tidal elevation measurements from tide gauges along the Antarctic coastline during the period 1900 to 1980. Restricted by the orbits of 66° latitude cut-off and sea ice coverage, the satellite altimeter measurements from TOPEX/Poseidon and Jason are not available for the Antarctic coastal regions. However, ocean tidal displacements can be estimated from ice shelf

surface displacements, if the observations are in hydrostatic equilibrium and far away from the grounding zone (Fricker et al., 2009).

Recently, the state-of-the-art in ocean tidal measurements and influences on ice shelves around Antarctica have been well documented by Padman et al. (2018). The excellent review of Padman et al. (2018) summarized the modern methods for measuring ice shelf tidal elevations by Global Positioning System (GPS), satellite altimeter measurements including radar altimeters and laser altimeters, satellite gravity measurements, and synthetic aperture radar. With the aid of the sufficient dataset of tidal elevation measurements, the accuracies of Antarctic tidal models can be substantially improved. However, tidal currents rather than height variability may play a dominant role in affecting the basal mass balance of ice shelves (MacAyeal, 1984; Makinson and Nicholls 1999; Galton-Fenzi et al., 2012).

With the aid of the conventional oceanographic moorings deployed on the Antarctic continental shelf, tidal-resolving current records in the shelf sea have been obtained during the past several decades. Johnson and Van Woert (2006) documented the current meter moorings deployed in the Ross Sea during the period 1980 to 1998, including three moorings near the Ross Ice Shelf front (Pillsbury & Jacobs, 1985). They highlighted the seasonal and interannual variability of the tidal currents. Semper and Darelius (2017) summarized the moorings with tide-resolving current meters in the Weddell Sea during the period 1968 to 2014, including four moorings near the Ronne Ice

Shelf front. They emphasized the summer enhancement of diurnal tidal currents at the shelf break induced by the resonance of coastal trapped waves. Compared to the extensive observations of tidal currents in the Ross and Weddell seas, tidal currents have not been well described in Prydz Bay, the third largest bay around Antarctica (Figure 1).

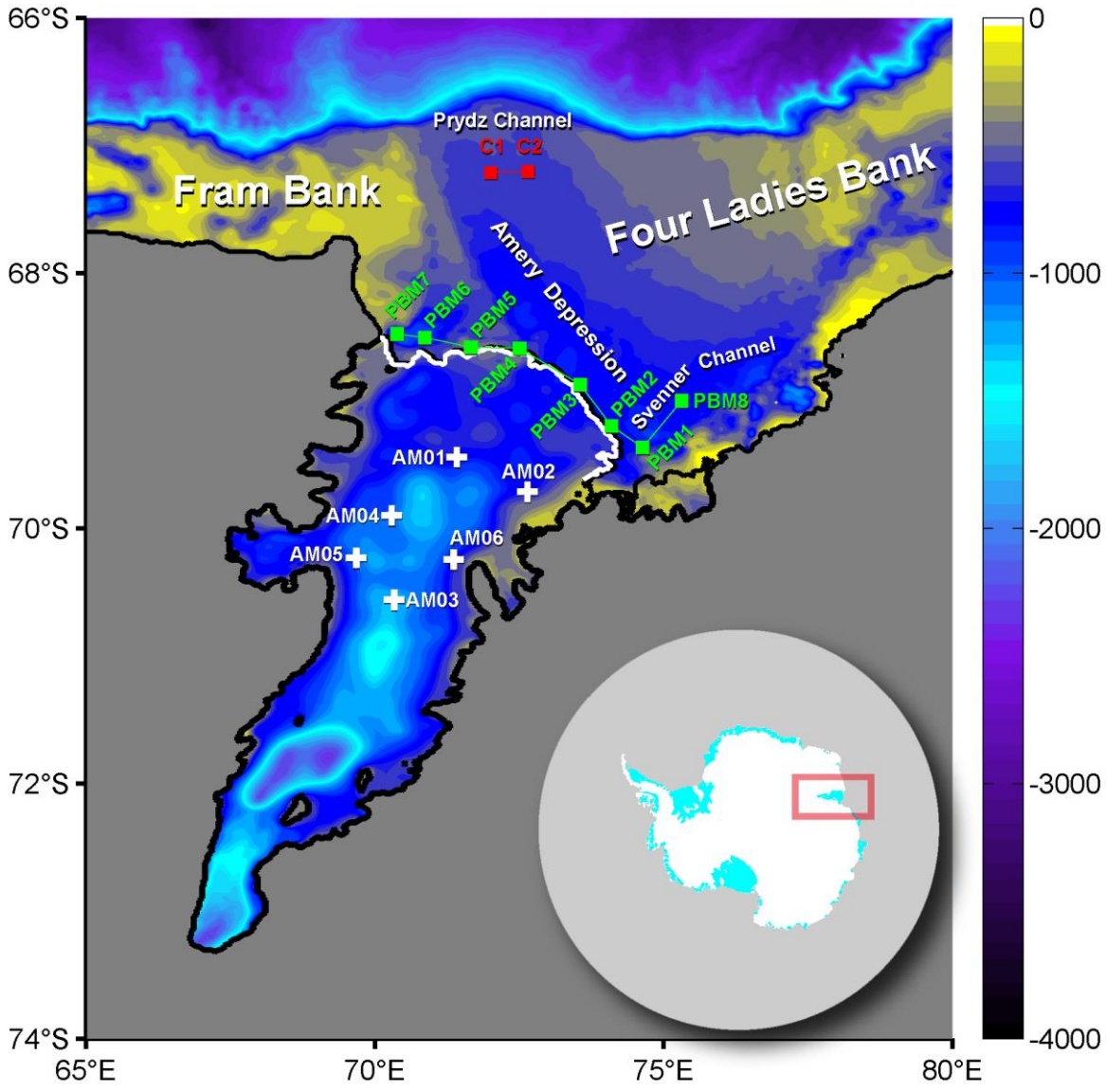

Figure 1. Topographical features from RTopo-2 in Prydz Bay (m). The red box in the lower inset shows the location of our region of interest. The Chinese Antarctic Expedition (CHINARE) moorings (red squares) are labeled by C1 and C2. The AMISOR moorings (green squares) are labeled by PBM1-PBM8. The AMISOR borehole sites (white pluses) are labeled by AM01-06. The thick white line shows the Amery Ice shelf (AIS) calving front.

Indeed, previous observational studies focused in Prydz Bay have already illuminated the tidal influences on the Amery Ice Shelf (AIS), the third-largest ice shelf around Antarctica. Based on an airborne reconnaissance, Mellor and McKinnon (1960) firstly reported large parallel cracks or crevasses on the AIS, presumably due to tidal shear forces. King et al. (2000) first post-processed the vertical displacement of the AIS measured by GPS receivers, and they reported spurious periodic signals from GPS time series (King et al., 2003), due to the presence of tidally-induced vertical ice surface oscillation. By assessing the vertical oscillations of free-floating AIS in response to tides, Fricker et al. (2009) firstly developed a benchmark map for the AIS grounding zone from a combination of satellite data. Additionally, one continuous 7-hour record from an acoustic current meter deployed at a borehole site drilled through the AIS showed an initial inflow swinging to a steady outflow about 3 h later (Craven et al., 2004), implying that the observed currents in cavity might be dominated by tides (Padman et al., 2018). In reality, tidal currents rather than height variability play a more dominant role in affecting the basal mass balance of ice shelves (MacAyeal, 1984; Makinson and Nicholls 1999; Galton-Fenzi et al., 2012), stressing the importance of tidal current measurements in Prydz Bay.

The long term tidal current measurements are so limited that previous investigations focused on the tidal currents in Prydz Bay are mostly based on numerical models (Galton-Fenzi et al., 2012; Hemer et al., 2006; Maraldi et al., 2007). By

employing a barotropic tidal model (1/10°× 1/30°), Hemer et al. (2006) described the simulated tidal amplitudes and phases of the main tidal constituents in detail, consistent with the simulated results from the Circum-Antarctic Tidal Simulation (Padman et al., 2002), and Hemer et al. (2006) proposed that the barotropic tidal mixing had little influence on the AIS basal melting due to the weak tidal currents. However, Galton-Fenzi et al. (2012) suggested that the simulated tides could lead to large fluctuations in the ocean heat content of the AIS cavity and consequently play an important role in the AIS basal mass balance. The different results in previous modeling studies are probably due to the large uncertainties of the simulated tides in polar regions (Padman et al., 2018; Ray et al., 2019). Dominant sources of uncertainties may result from uncertainties in the topography, model resolution, and open boundary conditions. For example, the tidal currents applied at the open boundary conditions in Galton-Fenzi et al. (2012) are provided by a simple analysis tidal signal data set from Murray (1964). The uncertainties of the tidal boundary conditions are largely dependent on the accuracy of the tidal currents prescribed at the open boundaries (Jourdain et al., 2019). Recently, the coupled ocean-sea ice-ice shelf modeling studies focused on Prydz Bay also showed some significant deficiencies due to the omission of tides in the ocean model (Liu et al., 2017; 2018). Therefore, the quantitative assessments of the tidal currents and corresponding changes and tidal heat transports in Prydz Bay are particularly informative in better understanding the tidal influences on the AIS basal mass balance in Prydz Bay.

The principal aim of this study is to assess the direct tidal current observations in Prydz Bay. So far, the directly observed tidal currents near Prydz Bay have only been documented by Ohshima et al. (2013). As such, based on the long-term mooring arrays deployed in Prydz Bay, we aim to quantitatively describe the observed tidal currents and ellipses on the continental shelf. We also analyzed the vertical structure of changing tidal currents along the AIS calving front, with corresponding tidal heat transport. Furthermore, we preliminarily outline the potential tidal influences on the AIS basal melting based on hydrographic observations of borehole sites drilled through the AIS.

The paper is organized as follows. Section 2 provides descriptions of the hydrographic observations and the methods used for assessing the tidal currents. A detailed evaluation of the observed tidal currents and potential impacts on the AIS are presented in section 3. Section 4 summarizes and provides a discussion of the results.

2 Data and Methods

2.1 Hydrographic Data and Modeling Data

The observational data used in this study were from 10 moorings over the continental shelf and six borehole sites drilled on the AIS. The mooring array consists of 2 moorings in the Prydz Channel (71-73.5°E), 7 moorings along the AIS calving front (70.4-74.6°E), and 1 mooring in the Svenner Channel (75.3°E; Figure 1). The latest topographic dataset RTopo-2 (the Refined Topography data set; Schaffer et al., 2016)

was used to provide the reference seafloor depth and ocean cavity geometry for our interpretation of the spatial distribution of the observational sites.

The moorings near the AIS calving front were deployed as part of the Amery Ice Shelf Ocean Research (AMISOR) from February 2001 and recovered in February 2002 (Figure 2a). In this study, we named these moorings from the AMISOR as PBM1 to PBM8 by following the previous literatures (Herraiz-Borreguero et al., 2016; Herraiz-Borreguero et al., 2015). Twenty-five rotor current meters were equipped on the AMISOR moorings, besides one acoustic current meter on PBM7. The AMISOR mooring array was deployed along the AIS calving front, except that PBM8 was located in the Svenner Channel (Figure 1). The details of the AMISOR mooring array design have been documented in Herraiz-Borreguero et al. (2016), with the data quality-control processes described in Herraiz-Borreguero et al. (2013; 2015). It is worth noting the significant discrepancy between the observed bathymetry and that in RTopo-2 (Figure 2).

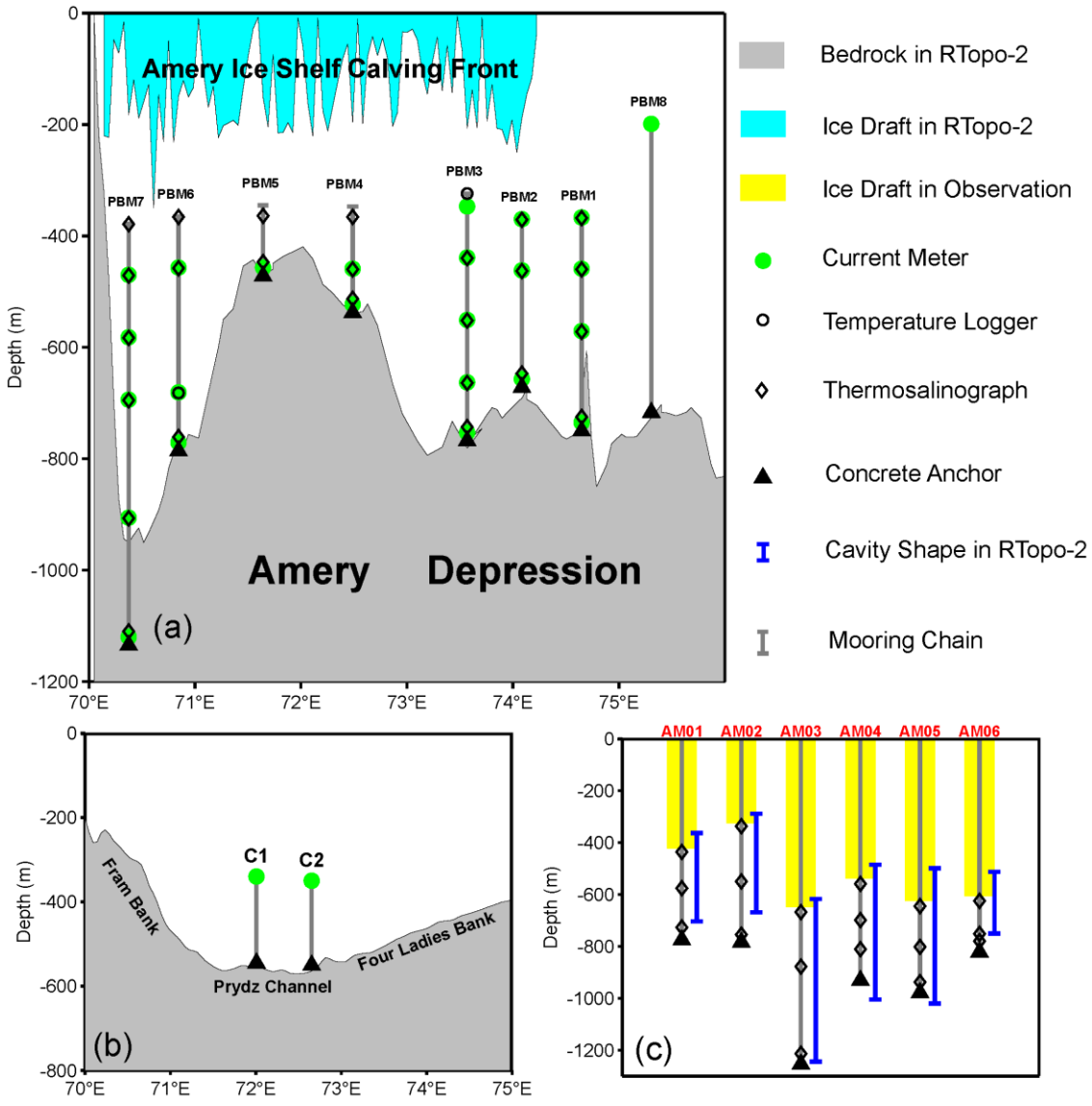

Figure 2. (a) The cross-section of the AMISOR moorings along the AIS calving front (green squares shown in Figure 1), with the topography from RTopo-2. (b) The CHINARE moorings in Prydz Channel (red squares shown in Figure 1). (c) The moorings deployed through the AMISOR boreholes (white pluses shown in Figure 1).

Two moorings (hereafter called C1 and C2) were deployed in the Prydz Channel by the 29th Chinese Antarctic Expedition (CHINARE), equipped with electromagnetic current meters (Figure 2b). C1 was deployed in March 2013 and recovered in February 2015, and C2 was deployed in March 2013 and recovered in February 2015 (see Table S1 in the supplementary for the details of the CHINARE moorings design). The velocity data was averaged over 1-hour time intervals. The local magnetic declinations were used to calculate the real northward and eastward velocity directions. The accuracy of the electromagnetic velocity sensor is ±1 cm s^{-1} in magnitude and ±2° in direction. The submarine channels intersecting the continental shelf break have significant dynamic effects on the Antarctic Slope Current and favor the CDW intrusion from the abyssal ocean onto the continental shelf (St-Laurent et al., 2013). Stewart et al. (2018) also suggested that the simulated tidal currents could induce a strong onshore heat transport across the shelf break at the depth from 500 m to 1000 m, East Antarctica. Accordingly, C1 and C2 deployed in the Prydz Channel at ~550 m depths were designed to capture the cross-shelf water mass exchanges and associated tidal processes (Figure 1).

Six borehole sites, hereafter called AM01 to AM06, were hot water-drilled on the AIS as part of the AMISOR and operated from January 2001 to August 2011 (see Table S2 in the supplementary for the borehole sites design). In each borehole site, three thermosalinographs were deployed: adjacent to the ice shelf base, at the mid-depth of the cavity and over the seafloor, respectively (Figure 2c). Based on the hydrographic observations at these borehole sites, Herraiz-Borreguero et al. (2016) have described the

modified Circumpolar Deep Water (mCDW) intrusion at the northeastern flank of the AIS cavity. Based on the temperature and salinity records, we can assess the tidal influences on the seawater characteristics in the sub-ice-shelf cavity.

The simulated barotropic tidal currents from the Circum-Antarctic Tidal Simulation version 2008 (CATS2008), an inverse tide model, were compared with the observed tidal currents at each mooring station. CATS2008 is an update to the regional model developed by Padman et al. (2002), covering the entire Southern Ocean south of 56°S. The CATS2008 model assimilates a wide range of tidal height data from tide gauges, gravimeter measurements, TOPEX/Poseidon altimetry data, and the ICESat crossover data, with open boundaries driven by a global tides model TPXO5.1. It is worth noting that CATS2008 is a barotropic tidal model that is not coupled with sea ice evolution.

2.2 Analysis Methods

In this study, we carried out a harmonic analysis for the observed currents using the T_TIDE software (Pawlowicz et al., 2002) to obtain the tidal current amplitudes, phases (relative to Greenwich) and tidal ellipse inclinations of eleven tidal constituents.

With the harmonic analysis results, we further calculated the heat flux induced by the tidal currents and residual currents for each current meter as follows:

$$\vec{u}_r = \vec{u} - \vec{u}_t \tag{1}$$

$$F_{tide} = \vec{u}_t \cdot \left(T - T_f\right) \tag{2}$$

$$F_{res} = \vec{u}_r \cdot \left(T - T_f\right) \tag{3}$$

where $\vec{u}$ is the observed current, $\vec{u}_t$ is the tidal currents from harmonic analysis, $\vec{u}_r$ is the residual currents, T is the potential temperature from the thermosalinographs deployed near the current meter (Figure 2a), T_f is the freezing point temperature with the value of -2.8 °C (calculated on the basis of 34.5 psu and 1120 m depth where the deepest current meter is deployed), F_{tide} is the heat flux induced by tidal currents, and F_{res} is the heat flux induced by residual currents.

In order to quantify the tidal contribution to the total kinetic energy in Prydz Bay, we calculated the Tidal Kinetic Energy (TKE) and the Residual Kinetic Energy (RKE). The time-averaged TKE was computed as follows:

$$\overline{TKE} = \overline{\frac{1}{2}\left(u_t^{\,2} + v_t^{\,2}\right)} \tag{4}$$

where u_t and v_t are the analyzed zonal and meridional components of the tidal currents integrated over all tidal constituents, and the overbar indicates averaging over the entire observational period (typically one year, from February 2001 to February 2002). Then, the average RKE can be estimated by the residual currents:

$$\overline{RKE} = \overline{\frac{1}{2}\left(u_r^{\,2} + v_r^{\,2}\right)} \tag{5}$$

where the u_r and v_r are the zonal and meridional components of the residual velocity fields. The ratios of TKE and RKE to the total Kinetic Energy (KE) can provide a preliminarily, quantitative estimate of the relative importance of tidal currents in Prydz Bay.

3 Results

3.1 Phases, amplitudes and ellipses of tidal constituents

The T_TIDE analysis were applied to all the current meter records from moorings (see Table S3 in the supplementary for the detailed results of the T_TIDE analysis), and we showed the velocity of the zonal and meridional tidal currents at C1 as an example (Figure 3). The averaged magnitudes of zonal tidal currents were typically less than 5 cm s^{-1} (Figure 3a, b); however, the maximal zonal tidal currents reached 11 cm s^{-1}, twice as large as the typical velocity observed on the continental slope off Cape Darnley (Ohshima et al., 2013). Both of the zonal and meridional tidal currents showed an evident oscillation with a period of about two weeks, coinciding with the spring-neap time scale (~14.8 days) presented in the KE power spectrum (the peak noted by a green line in Figure 3c). The KE power spectrum also showed significant peaks in the short period band less than 30 hours (the green block in Figure 3c), exerting the lunar and solar tidal currents (Figure 3d). The most energetic diurnal, semi-diurnal, third-diurnal, and quarter diurnal constituents peak in the luni-solar diurnal period (K_1, 23.93 hours), the principal lunar semidiurnal period (M_2, 12.42 hours), the shallow water tridiurnal period (MO_3, 8.37 hours), and the shallow water quarter diurnal period (MS_4, 6.10 hours). The inertial period at the latitude of C1, ~12.98 hours, is nearly equal to the M_2 period, yet there was no significant spectral peak at that period (Figure 3d).

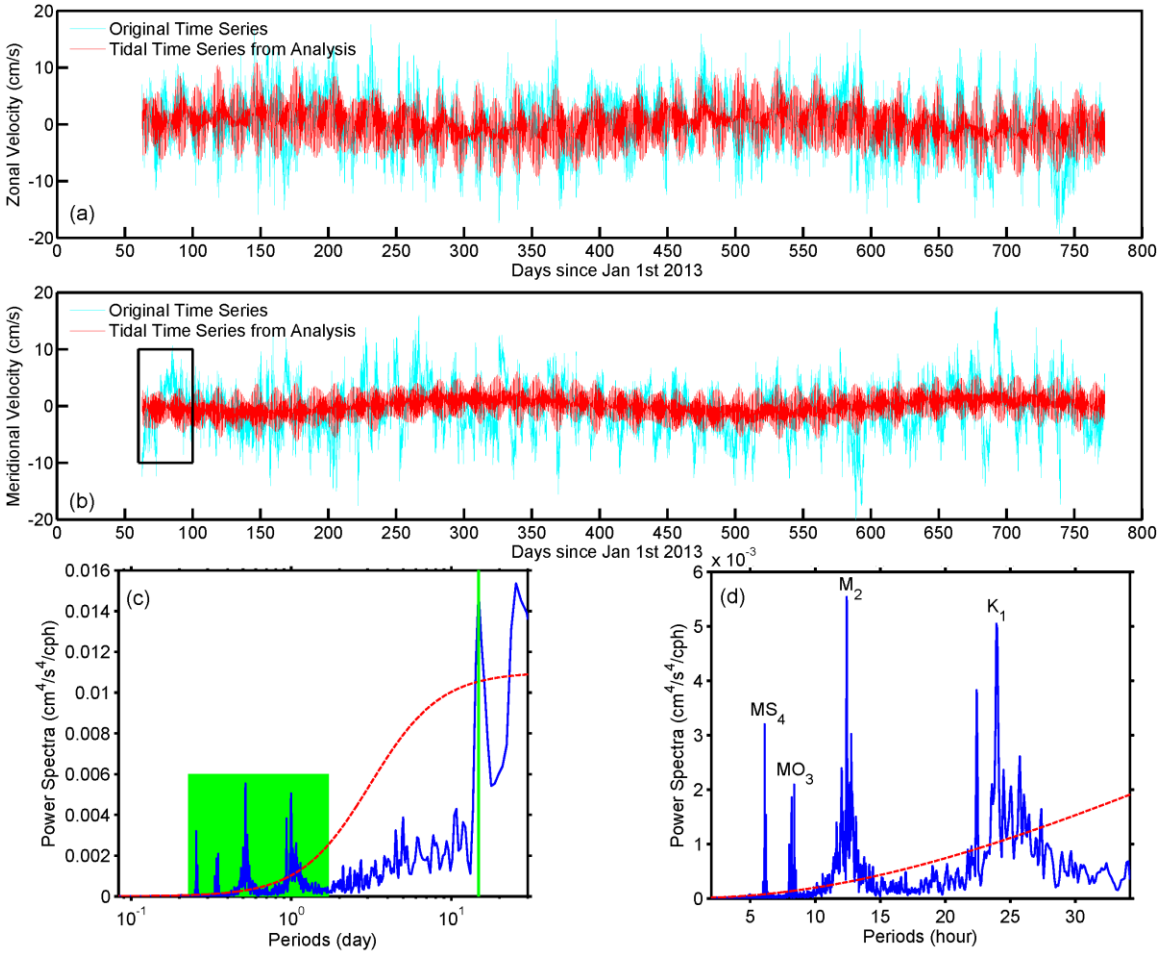

Figure 3. (a) The original zonal velocity (the Cyan line) and the harmonically analyzed tidal velocity (the red line) observed by the current meter (at 340 m depth) at C1. (b) is the same as (a), but for the meridional velocity. The black box in (b) denotes the enlargement shown in Figure 4a. (c) The power spectra (blue lines) of the KE at C1. The red dashed lines show the 95% confidence level. The green line denotes the spring/neap tide periods. The green block in (c) denotes the enlargement shown in (d). (d) is the same as (c), but focused on the high-frequency band to show the most significant diurnal, semidiurnal, third-diurnal, and quarter diurnal tidal energy.

In addition to the tidal currents, the T_TIDE analysis results also provide the phases and amplitudes of the significant tidal constituents. Although the observed tidal currents at C1 was stronger than on the continental slope (Ohshima et al., 2013), the amplitudes of the residual zonal currents were still about twice as large as the zonal tidal currents (Figure 4a). The semidiurnal and diurnal tidal constituents were most significant (Figure 4b), with the four tidal constituents M_2, O_1, K_1, and S_2. M_2, the principal lunar semidiurnal constituent (12.4 hours), was the largest component (Figure 4b). In order to diagnose whether the diurnal or semidiurnal tidal constituents are dominated, we computed the tidal current form factor, $F=(\text{major}(K_1)+ \text{major}(O_1))/(\text{major}(M_2)+ \text{major}(S_2))$, where major(•) is the maximal tidal velocity (the amplitudes shown in Figure 4b) of the corresponding tidal constituent. A large F value indicates that the local tidal currents are diurnally dominated, and vice versa. To reveal the spatial distribution of the tidal current form factor in Prydz Bay, we calculated the F value of the T_TIDE analysis results from all of the current meter records. F at C1 was about 0.96, and the average F for all the current meter records was 0.84, indicating that the diurnal tidal currents were a little weaker than the semidiurnal tidal currents over the outer continental shelf. As expected, the energetic peaks in the rotary spectrum were in the diurnal, semidiurnal, and third-diurnal frequency (the red lines in Figure 4c), and there was still little energy in the inertial frequency that is on the positive flank of the rotary spectrum in the southern hemisphere (the green line in Figure 4c).

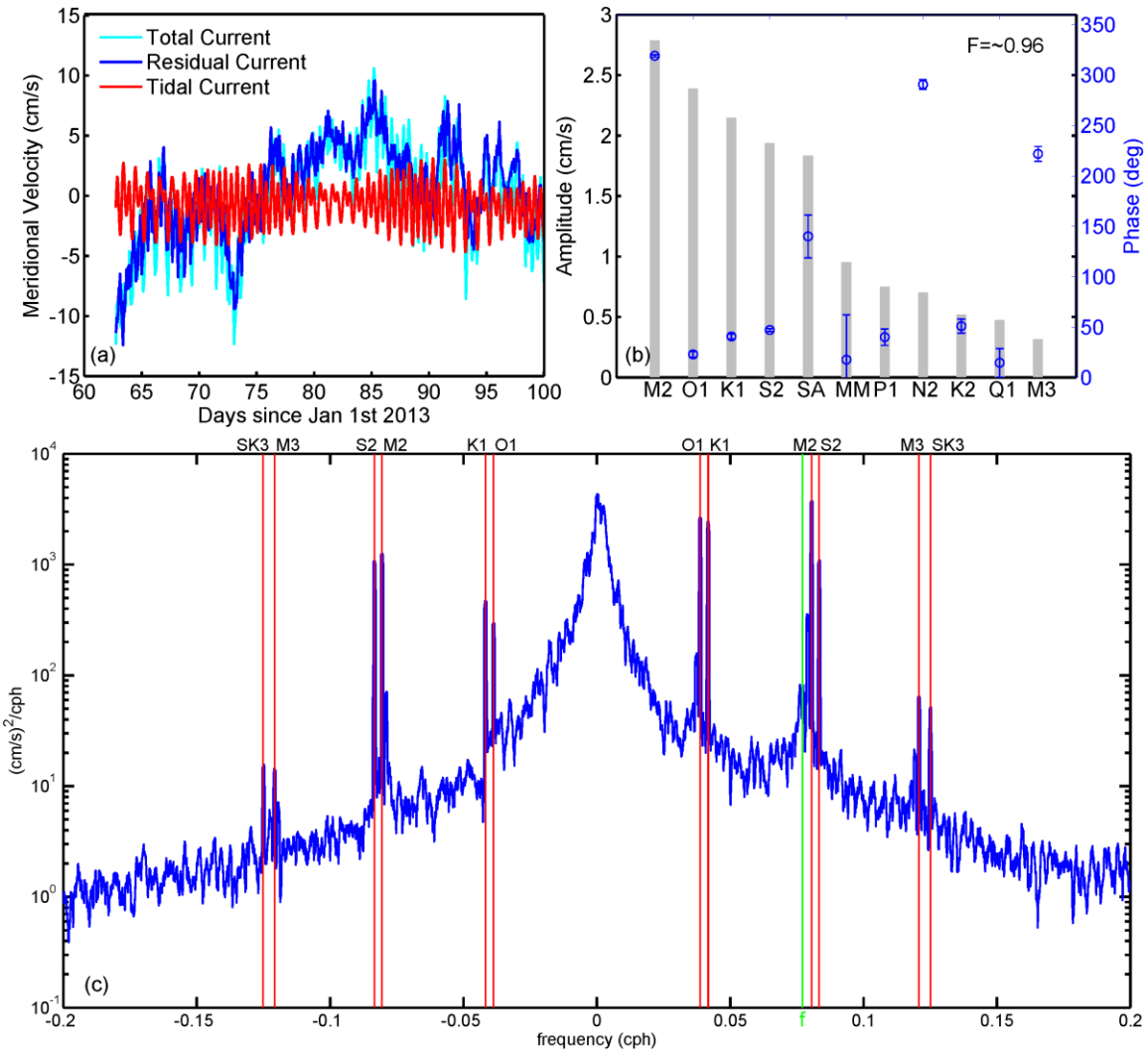

Figure 4. (a) The enlargement of the original zonal velocity, residual velocity and tidal velocity over the first 100 days (the black box shown in Figure 3b) observed by the current meter at C1. (b) The amplitudes (the maximal tidal velocity; grey bars) and phases (blue circles) of the harmonic analyzed tidal constituents. The blue error bars indicate the 95% confidence interval of tidal phases. F value is the tidal current form factor. (c) The rotary spectrum of the velocity observed at C1. The red lines show the frequency of the main tidal constituents M_2, O_1, K_1, and S_2. The green line denotes the frequency of the inertial oscillation.

331 In order to delineate the temporal evolution and horizontal distribution of the tidal
332 currents over the continental shelf, we assessed the tidal ellipses for the primary tidal
333 constituents based on the records from the shallowest current meter on each mooring,
334 with the corresponding depths ranging from 199 m (PBM8) to 470 m (PBM7). The
335 semi-major axes of the M_2 tidal ellipses derived from the shallowest current meters were
336 all less than 3 cm s^{-1} over the continental shelf (blue and red ellipses in Figure 5), with
337 the maximum of 2.79 cm s^{-1} for the M_2 constituent at C2. The averaged semidiurnal
338 semi-major axis along the AIS calving front was approximately 1.5 cm s^{-1} for the M_2 and
339 S_2 constituents, and 1.1 cm s^{-1} for the diurnal K_1 and O_1 constituents (see Figure S1 in the
340 in the supplementary for details). Essentially, the magnitudes of the semidiurnal currents
341 were slightly larger than those of the diurnal currents, and the tidal ellipses were mostly
342 cyclonic, except at the C2, PBM3, and PBM4. The smallest semi-major axis (0.39 cm s^{-1})
343 was observed in the Prydz Channel for the M_2 constituent. The alignments of the
344 principal axis of the semidiurnal and diurnal tidal ellipses were generally north-south in
345 the Prydz Channel and perpendicular to the AIS calving front. At the AIS calving front,
346 the maximal tidal currents for the semidiurnal constituents were identified at PBM4 and
347 PBM5, yet the maximal tidal currents for the diurnal constituents occurred at PBM5 and
348 PBM7 (see Table S3 in the supplementary for details). It is interesting to note that PBM1,
349 PBM2, and PBM3 were located at the intrusion path through which mCDW was
350 transported into the AIS cavity, implying that the observed tidal currents may have
351 potential influences on the AIS basal mass melting by bringing warm mCDW into the

AIS cavity. The simulated barotropic tidal ellipses from CATS2008 (green and yellow ellipses in Figure 5) were not in close agreement with the observed tidal ellipses from moorings, implying the potential uncertainties in the Antarctic tide models (Ray et al., 2019). Importantly, CATS2008 is a barotropic tide model with only barotropic tidal currents predicted, and thereby the discrepancy between observation and CATS2008 is probably due to the baroclinic tidal currents in observation. Around the Antarctic continent, the tidal phase generally propagates from the east to the west. The non-monotonic changes in the tidal phases along the AIS calving front may also underline the influences of baroclinic tidal processes (Figure 5).

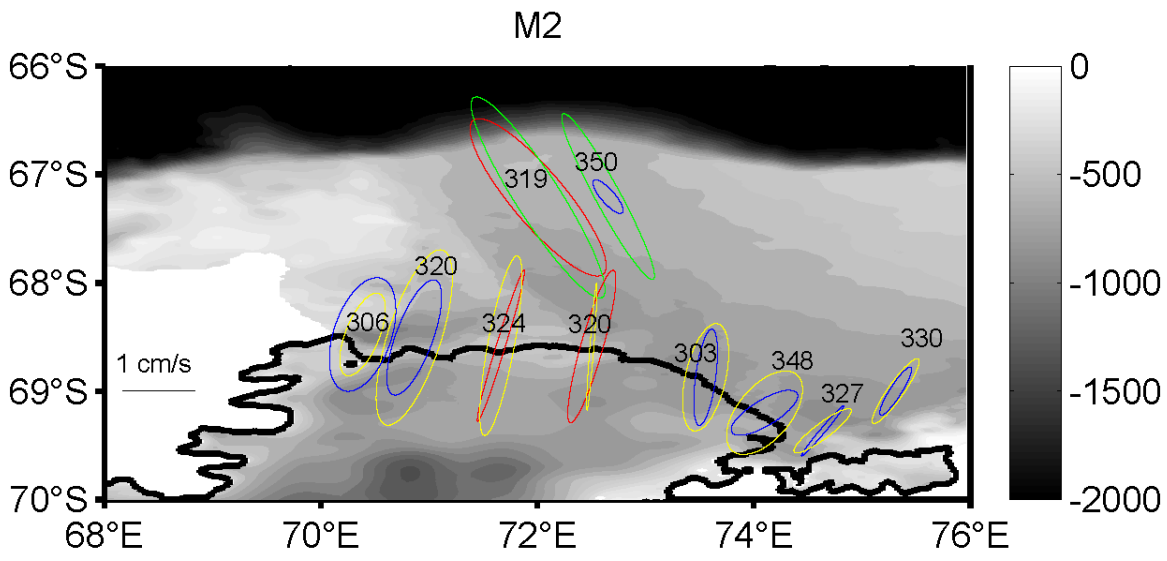

Figure 5. The tidal current ellipses of the M_2 constituent from the shallowest current meters equipped on the AMISOR moorings along the AIS calving front and the moorings at C1 and C2 (the deployed depths of current meters ranges from 312 m to 470 m; see Table S1 and Table S3 in the supplementary for details), with the corresponding phases (the numbers at the tidal ellipses in degrees). Red ellipses are anticyclonic, and blue ellipses are cyclonic. The simulated barotropic tidal current ellipses from CATS2008 are also presented with green ellipses (anticyclonic) and yellow ellipses (cyclonic).

The AMISOR moorings along the AIS calving front (from the westernmost PBM7 to the easternmost PBM1) provided an opportunity to assess the vertical structure of the tidal currents for the main tidal constituents along the AIS calving front (Figure 6). There were no evident changes in the tidal ellipses for the four main tidal constituents with depth, implying that the tidal currents along the AIS front were primarily barotropic, except at PBM7. The increasing inclinations of the ellipse principal axes with depth at PBM7 appeared to be induced by the baroclinic tidal components, suggesting the spatial asymmetry of the tidal currents at the AIS calving front. In principle, the cyclonic rotation of tidal ellipses with depth at PBM7 probably indicated the dynamic response of the vertical tidal currents shear to the steeply deepening topography (Figure 2a), i.e., due to the generation of internal tides (Padman et al., 2006). For the M_2, O_1, K_1, and S_2 constituents, the maximal tidal currents were observed at PBM5 (current meter deployed at 457 m depth), decreasing on both the east and west sides. The simulated tidal ellipses from CATS2008 (black dashed lines in Figure 6) were of similar inclinations to the mooring observations at PBM3, PBM6, and PBM5, with some discrepancies at PBM2 and PBM4. The eccentricities (the ratio of semi-minor axis over the semi-major axis) were similar, except at PBM1. Apart from the misfit at PBM7 where there are strong baroclinic tidal currents, as a barotropic tide model, CATS2008 still can provide benchmark results for the tidal forcing of ocean models.

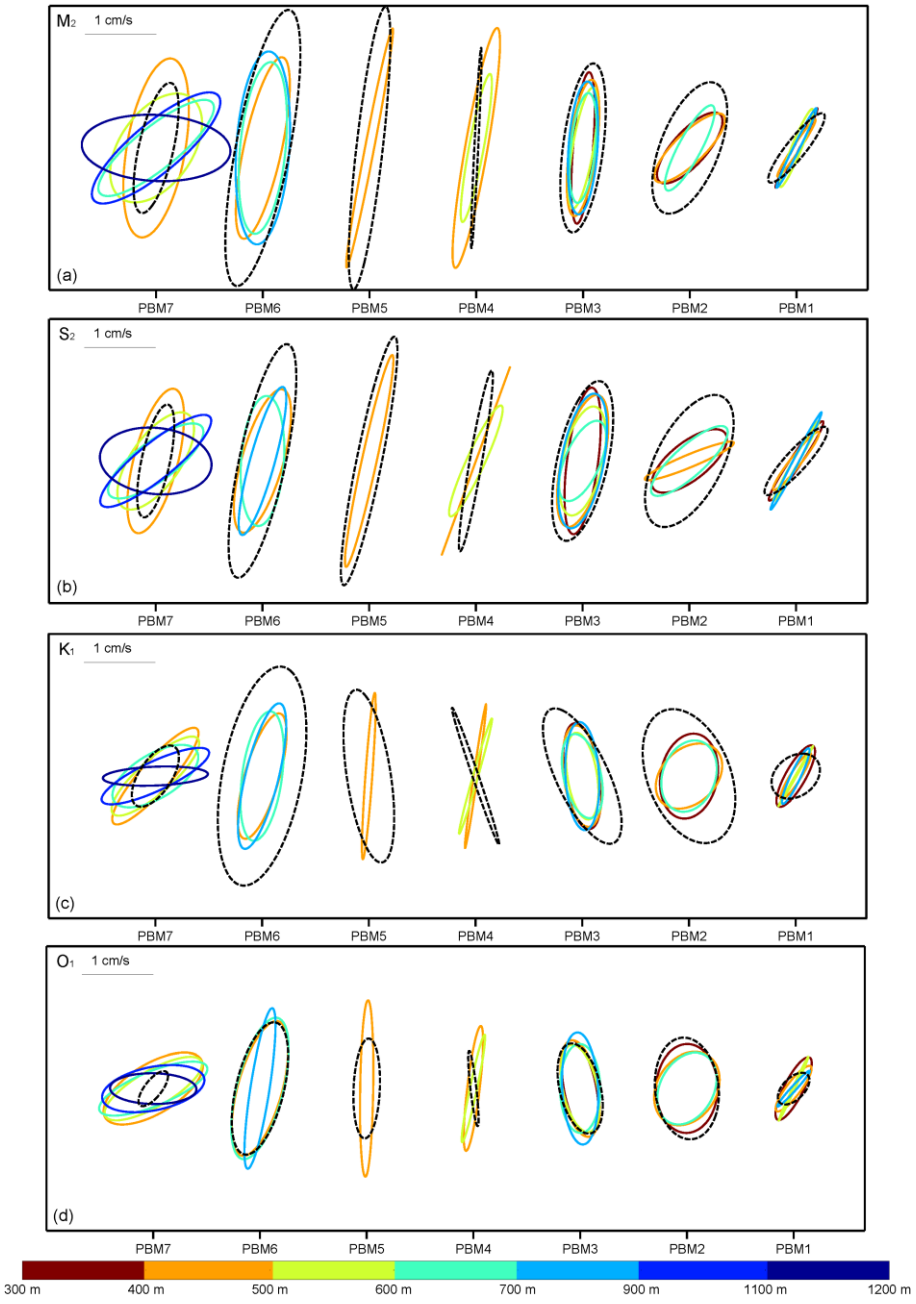

Figure 6. The tidal ellipses of the (a) M_2, (b) S_2, (c) K_1, and (d) O_1 constituents for the current meters equipped on the moorings along the AIS calving front. Each tidal ellipse is color coded according to the depth at which the measurements were sampled. The black dashed lines show the simulated barotropic tidal current ellipses from CATS2008.

3.2 Kinetic energy

Before we document if the tidal currents in Prydz Bay can play an important role in the heat transport and the AIS basal mass balance (Hemer et al., 2006; Herraiz-Borreguero et al., 2016; Galton-Fenzi et al., 2012), it is instructive to conduct a quantitative assessment of the proportion of the $\overline{\mathrm{TKE}}$ in Prydz Bay. The harmonic analysis results for velocity fields showed the amount $\overline{\mathrm{TKE}}$ that can be accounted for in the $\overline{\mathrm{KE}}$ (Figure 7). The highest $\overline{\mathrm{TKE}}$ proportion even reached 32% at C1 in the center of the Prydz Channel, and the lowest $\overline{\mathrm{TKE}}$ proportion only accounted for 2% at PBM8 in the Svenner Channel. On the whole, the observed $\overline{\mathrm{TKE}}$ accounted for about 13% of the total $\overline{\mathrm{KE}}$ at the AIS calving front, with a maximum up to 25% at PBM3 (Figure 7). In agreement with the observed weak tidal currents off Cape Darnley by Ohshima et al. (2013), the averaged magnitudes of the tidal currents over the continental shelf were likely to be so weak (~ 2.58 cm s^{-1}) that they may not make a direct contribution to the AIS basal melting (Herraiz-Borreguero et al., 2016). However, the observed mean velocity at the AIS calving front from PBM1-7 was only 7.16 cm s^{-1}, with a maximum of 14.16 cm s^{-1} at the top layer of PBM7, implying the residual currents were also not very strong. In addition, the observed maximal tidal currents reached 13.12 cm s^{-1} at the PBM 7 at a depth of 694 m. Considering the ratios of $\overline{\mathrm{TKE}}$ and $\overline{\mathrm{RKE}}$ to $\overline{\mathrm{KE}}$, the observational records confirmed the simulated results in Galton-Fenzi et al. 2012 that the tides can induce significant oscillation in the heat content in the AIS cavity. Therefore, we suggest

416 that the contribution of the tidal processes should not be omitted in consideration of the
417 influences on the AIS basal mass balance. Compared to the observed $\overline{\mathrm{TKE}}$ in Prydz
418 Channel and at the AIS calving front, the simulated results in a high resolution (~1 km)
419 general circulation model still showed a stronger averaged $\overline{\mathrm{TKE}}$ bias (Stewart et al.,
420 2018), highlighting the uncertainty in the simulated tides in Prydz Bay.
421

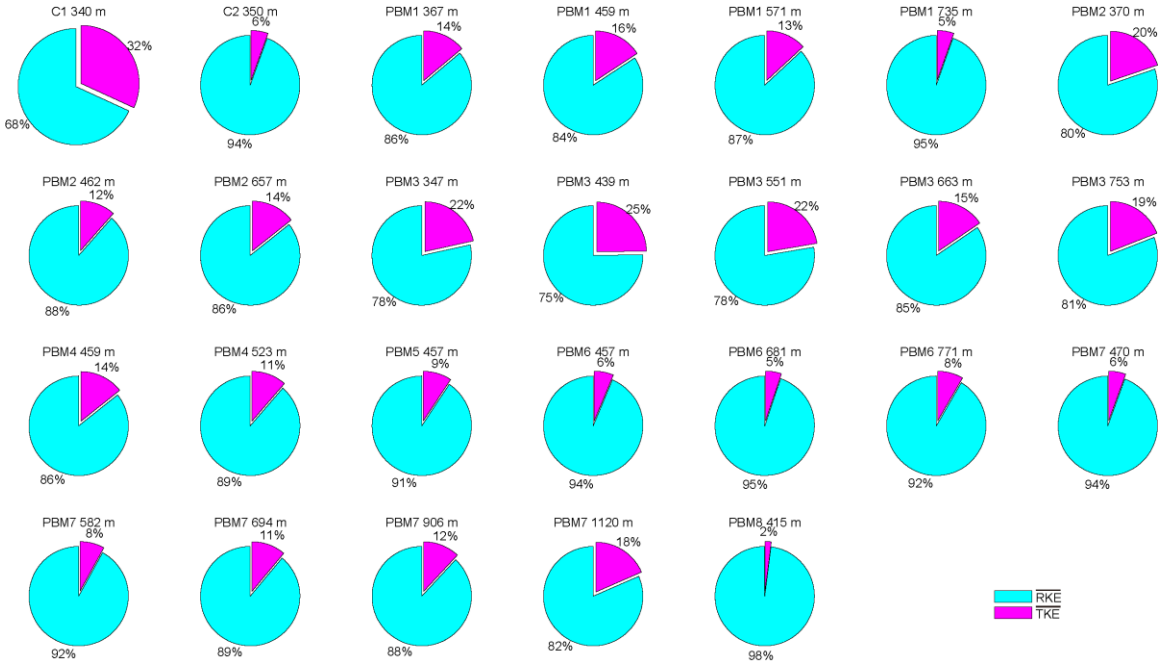

422

423 **Figure 7.** The proportions of average TKE and RKE in the total KE for all of the

424 current meters.

425

3.3 The seasonality of tidal currents

Driven by the astronomical forcing, tidal currents vary on regular time-scales, yet changes in tidal currents can be induced by the non-astronomical factors. Haigh et al., 2020 comprehensively reviewed the changes in tidal properties over multiple time scales and highlighted the responsible mechanisms such as water depth, coastline position, sea ice coverage, sea bed roughness, ocean stratification, and so on. In the Antarctic marginal sea, the changes in tidal currents may be primarily attributed to the variations in the extent of the sea ice cover, the geometric configuration of the ice shelf and oceanic stratification.

Since the observational records span about 1 year, we assessed the seasonality of the tidal currents rather than long-term changes. In this study, the summer period is December, January, and February; autumn is March, April, and May; winter is June, July, and August; and spring is September, October, and November. The changes in tidal currents can be classified by the changes in the length of the semi-major axes, the eccentricity and the inclination of tidal ellipses. For the M_2 constituent, the most stable tidal currents were found at C1 (Figure 8), with nearly no changes in any factors of the tidal ellipses between different seasons. The most significant changes were identified at PBM1, at depth 681 m, with remarkable seasonal variability in the semi-major axes, the eccentricity and the inclination of tidal ellipses. Generally, the seasonal variability in the eccentricity rather than in the semi-major axes or the inclination could be clearly

identified in the tidal ellipses of the remaining current meter records. Similar results could also be found in the tidal ellipses of the S_2, K_1 and O_1 constituents (see Figure S2-S4 in the supplementary), with relatively larger variability in the length of the semi-major axes. Considering the spatial asymmetry of the tidal currents at the AIS calving front, we also assessed if there are changes in the barotropic characteristic of the tidal currents. As expected, the significant baroclinic tidal currents of the M_2 constituent were only observed at PBM7, near the western corner of the AIS front (Figure 9), indicating that the internal tides observed at PBM7 may be correlated with the abrupt deepening in the bathymetry rather than the oceanic stratification (see Figure S5-S7 in the supplementary for the similar result of the S_2, K_1, and O_1 constituents). The rotary spectrum of the velocity observed by the shallowest current meters of the moorings at the AIS calving front showed evident peaks at the diurnal and semidiurnal tidal frequency band, with relatively weak diurnal energy levels at the positively-rotating spectra (Figure 10). The differences of the tidal energy peaks between different seasons suggested an apparent seasonality of tidal currents. Generally, the tidal energy peak was weakened in summer and intensified in spring (see Figure S8 in the supplementary for the rotary spectrum of all the remaining current meter records).

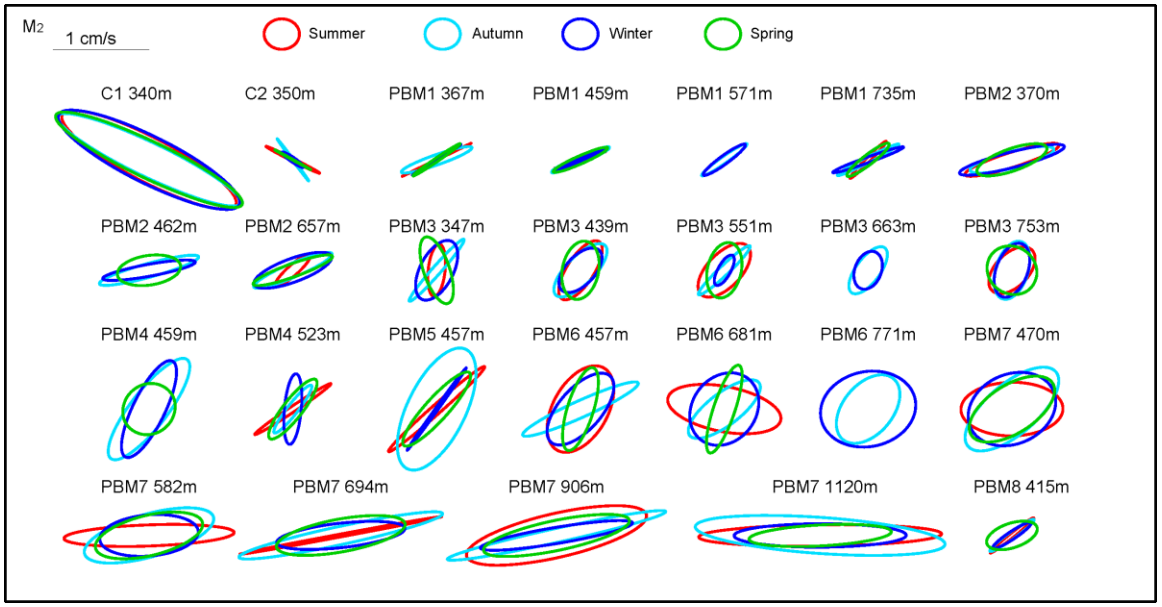

Figure 8. The tidal ellipses of the M_2 constituent for the current meters. Each tidal ellipse is color coded according to the season when the measurements were sampled.

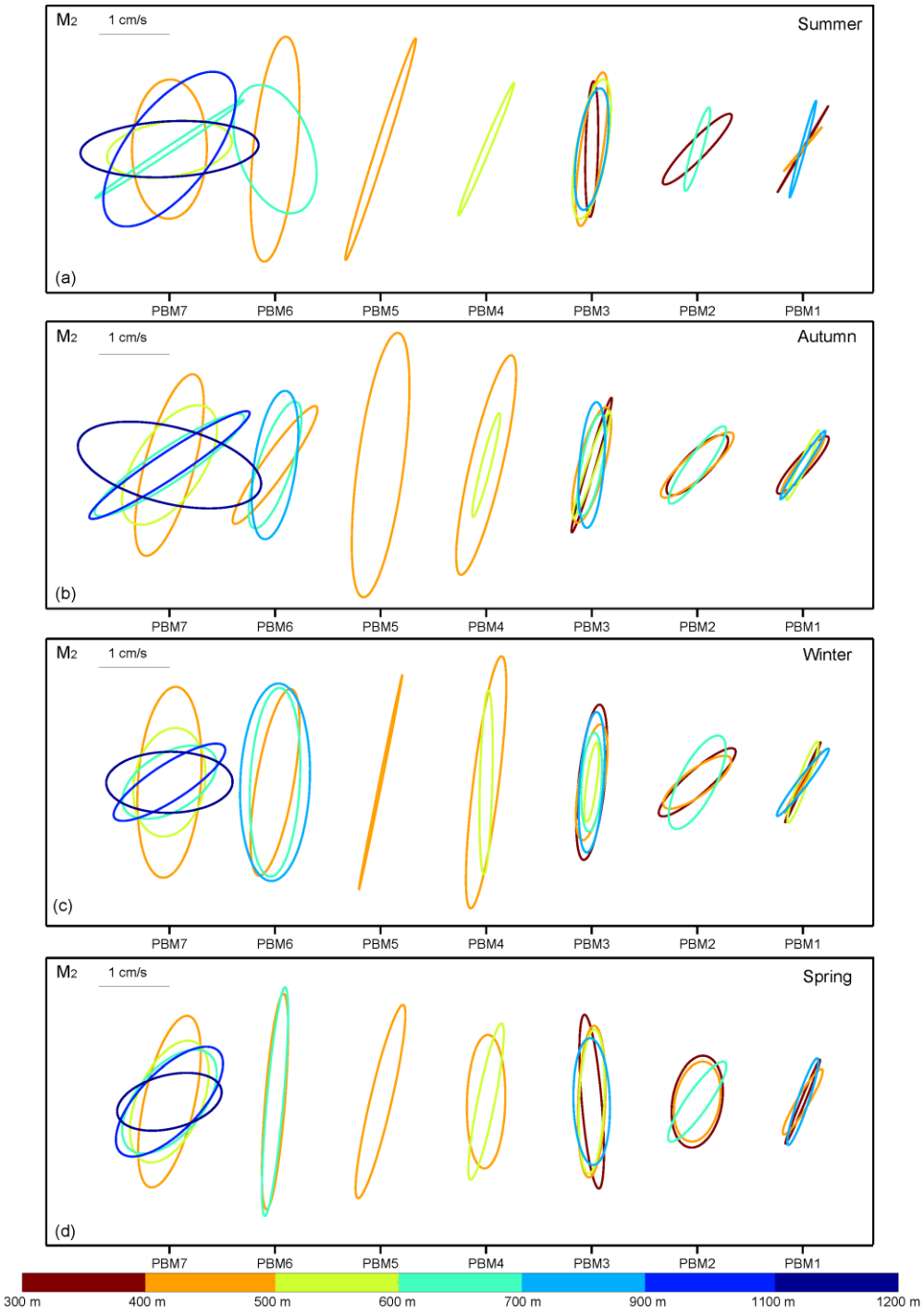

Figure 9. The tidal ellipses of the M_2 constituent for the current meters equipped on the moorings at the AIS calving front in (a) summer, (b) autumn, (c) spring, and (d) winter. Each tidal ellipse is color coded according to the depth at which the measurements were sampled.

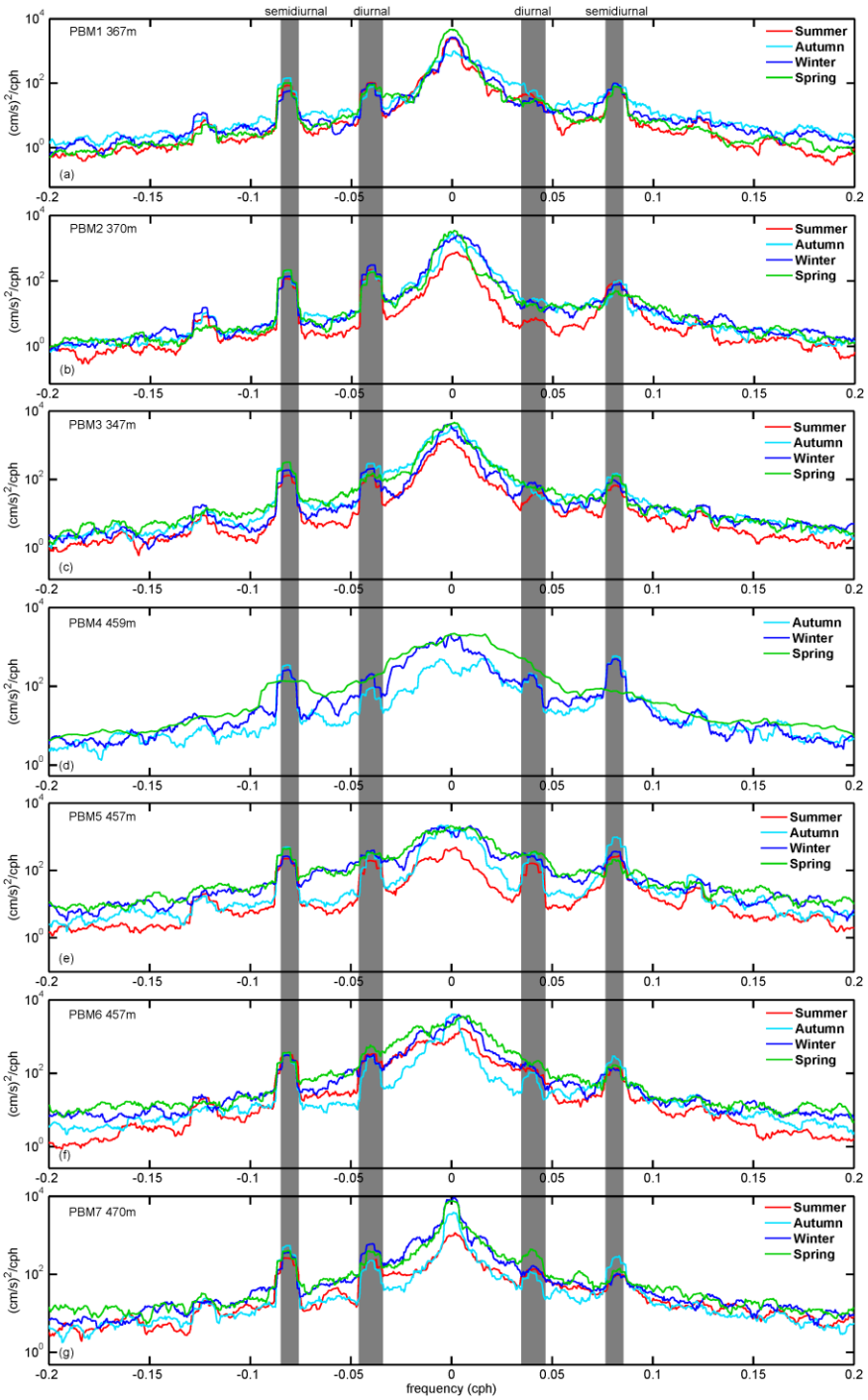

Figure 10. The rotary spectrum of the velocity observed at the shallowest current meters of the moorings at the AIS calving front. The diurnal and semidiurnal tidal frequency band is marked in grey. Each line is color coded according to the season when the measurements are sampled.

Here, we try to briefly discuss the potential mechanisms responsible for the seasonality of tidal currents in Prydz Bay. Tidal variability can be induced through interactions between the sea ice and the surface tidal currents on a seasonal timescale by increased friction at the ice-ocean interface during times of sea ice (St. Laurent et al., 2008; Müller et al., 2014). The tides can also be influenced by the changes in the extent of ice shelves and the shape of the ocean cavities; however, the corresponding timescale is usually longer than seasonal periods. In addition, changes in ocean stratification can aid the seasonal variability in tidal currents by changing the transfer energy from barotropic to baroclinic tides. The ocean stratification in Prydz Bay is comprehensively determined by the sea ice evolution, the mCDW intrusion (Herraiz-Borreguero et al., 2016; Liu et al., 2017), and the AIS basal melting (Galton-Fenzi et al., 2012) on seasonal timescales (see Figure S9 in the supplementary for the ocean stratification observed at the AIS calving front). Though we were hampered to quantitatively study what the dominant role is in regulating the seasonality of the tidal currents, yet our assessment might provide useful insights for future modeling studies focused on Prydz Bay.

3.4 Heat transport

To preliminarily examine the potential tidal contribution to the AIS basal mass balance, we first assessed the heat flux induced by the mooring observed tidal currents and residual currents, respectively. There was evidence that tide currents can modify the properties and circulation of water masses before they flow into the sub-ice-shelf cavity

by tidal mixing (Padman et al., 1992; Padman et al., 2009) and tidal rectification (Padman et al., 1992; Robertson et al., 1998) in the Ross Sea and the Weddell Sea. Considering the ratios of $\overline{\mathrm{TKE}}$ to $\overline{\mathrm{KE}}$ described in section 3.2, the tidal currents had the potential to significantly influence the characteristics and circulation of water masses in Prydz Bay. However, due to the very limited hydrographic data and the paucity of microstructure measurements, we cannot directly calculate the tidal contribution to mixing. To address this shortcoming, we calculated the heat flux at the AIS calving front to preliminarily evaluate if the tidal currents had the potential ability to induce significant oscillations of the heat content in the AIS cavity. Since the long term heat flux and consequent influences on the AIS basal melting has already been well documented in previous studies (Herraiz-Borreguero et al., 2015; Herraiz-Borreguero et al., 2016), here we only focused on the heat flux induced by tidal currents that have not been documented in Herraiz-Borreguero et al. 2016. As expected, the average tidal heat transport at the AIS calving front over the whole observational period was relatively small, with a typical value < 0.05 °C m s^{-1}, whereas the average zonal and meridional residual heat flux could be up to 0.42 °C m s^{-1} and 0.82 °C m s^{-1}, respectively (Figure 11). It was reasonable to find that the long term average of tidal heat flux was very small since the tidal currents are typically periodical oscillations. However, we found that the ratio of the tidal heat flux standard deviation to the residual heat flux standard deviation can be up to 41% (see Table S4 in the supplementary for the details). The salinity transport was also highly consistent with the heat flux (see Table S5 in the supplementary for the details). These

results indicated that tidal processes can resulted in significant oscillations in the heat content in the AIS cavity, confirming the simulated results in Galton-Fenzi et al. (2012). We agreed with Herraiz-Borreguero et al. (2016; 2015) that such periodic heat transport induced by tidal currents would not directly contribute to the ice shelf basal mass balance, yet the significant tidal oscillation in the AIS cavity may still enhance the AIS basal mass melting by enhancing mixing and heat content redistribution beneath the AIS. Therefore, the ice shelf basal melting induced indirectly by the tidal heat transport into the sub-ice-shelf cavity may start a density-driven current that can make a non-linear contribution to the ice pump cycle. Furthermore, in the western flank of the AIS cavity, the tidal oscillations can favor the transport and redistribution of the frazil ice generated by the ascending super-cooled ISW (Cheng et al., 2019; Cheng et al., 2017; Galton-Fenzi et al., 2012; Natalie 2011), which was important for both basal melting and marine ice accretion (refreezing). In section 3.5, we further diagnosed the hydrographic observations from borehole sites to show if the AIS basal surface can feel the oscillation in the heat content of the AIS cavity.

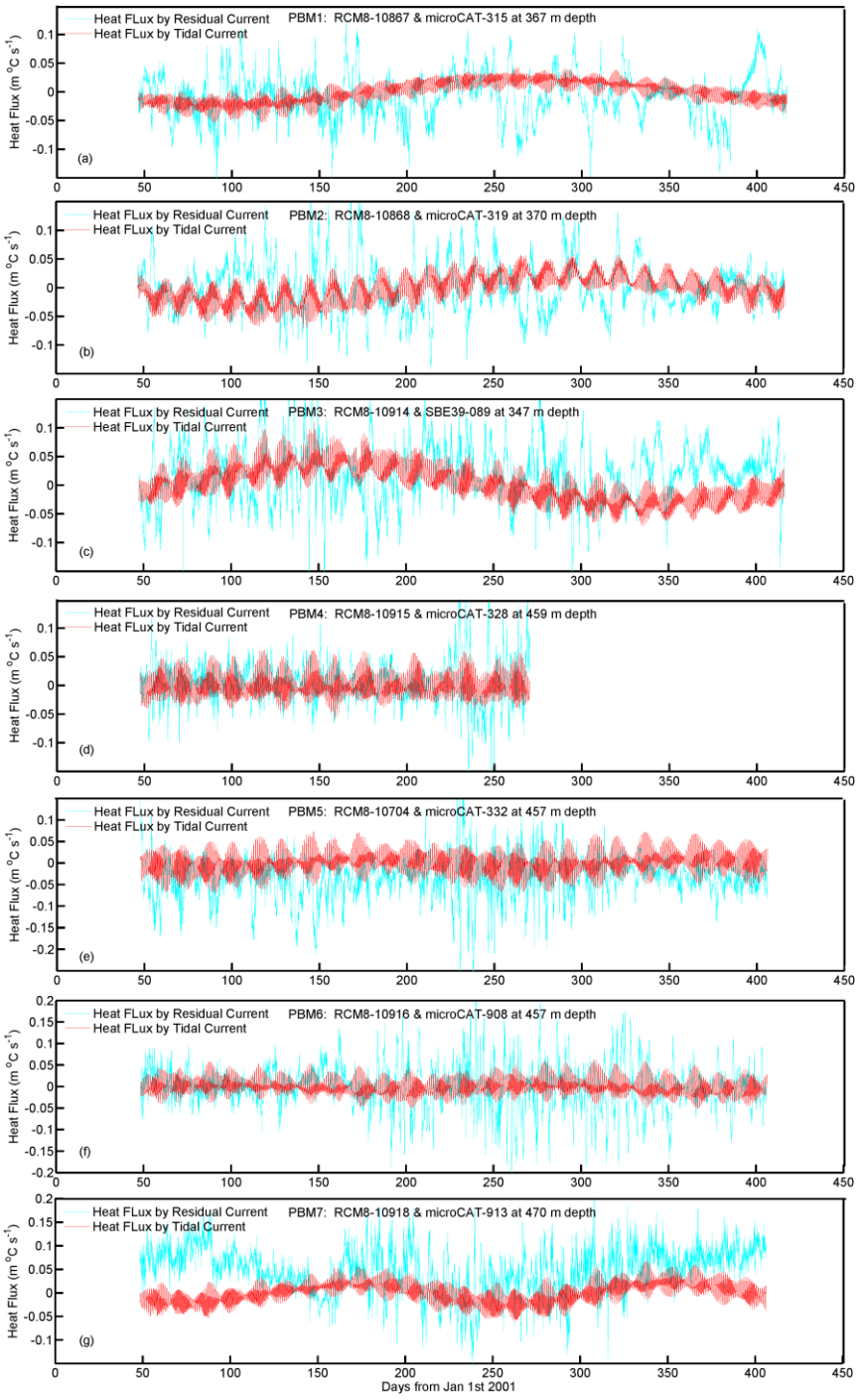

533

534 **Figure 11.** The heat flux (°C cm s^{-1}) at the shallowest current meters of the

535 moorings at the AIS calving front (the direction is perpendicular to the AIS calving front).

536 The cyan lines show the heat flux induced by the residual currents, and the red lines show

537 the heat flux induced by the tidal currents.

3.5 Tidal footprints beneath the AIS

In the ocean cavity, tides can modulate the ice shelf basal mass balance through their contribution to the thermal forcing (Hellmer and Olbers, 1989; Holland and Jenkins 1999), which is proportional to $\nabla T \cdot u^*$, where ∇T is the difference between the potential temperature and in situ freezing point; u^* is the friction velocity that is related with the turbulent kinetic energy in the ocean layer adjacent to the ice base. First, tidal currents can directly contribute to increased turbulence in the ocean layer beneath the ice shelf, especially in the cold cavity where the residual currents are weak. Second, the tidal modulation of the friction velocity in the boundary layer can induce changes in the temperature of the water masses through mixing, and thereby modify ∇T. For example, the Ross Ice Shelf and the Filchner-Ronne Ice Shelf basal melting have been proposed to be initiated by the small-scale turbulence induced by tidal mixing that brings denser SW to mix with ISW, and such mixture can come into contact with the ice shelf base (MacAyeal, 1984; Makinson & Nicholls, 1999; Robertson, 2016). Since there was no long-term current record in the AIS cavity, we had to focus on the tidal modulation of ∇T in the AIS cavity.

In order to diagnose tidal processes beneath the AIS, we analyzed the observed potential temperature and salinity over longer time-spans from six borehole sites. Compared to directly diagnosed current fields beneath the AIS, assessments of the potential temperature and salinity records were not a straightforward way to study the

558 evolution of tidal currents and the consequent influences on the AIS basal mass balance.
559 Unfortunately, the paucity of long-term velocity observations in the AIS cavity still
560 limited our ability to directly diagnose how the tidal currents evolve beneath the AIS.
561 Alternatively, we analyzed the observed records of the potential temperature and salinity
562 from 18 thermosalinographs deployed in the borehole sites (see Figures S9-S14 in the
563 supplementary for the full-time series of all the thermosalinograph records). These
564 potential temperature and salinity records may help us find the tidal footprints in the AIS
565 cavity.

566 By assessing the records of all the 18 thermosalinographs (see Figure S10-S15 in
567 the supplementary for the original time series), we found that 4 thermosalinographs at
568 four borehole sites (AM01, AM02, AM03, and AM06) captured significant oscillations
569 that may be coherent with tidal currents (the thin lines in Figure 12). AM02, AM06, and
570 AM03 were located in the eastern flank of the AIS where warm inflow could flow
571 through these three borehole sites (Figure 1). Consistent with the results of
572 Herraiz-Borreguero et al. (2015), warm mCDW were observed at AM02 (see Figure S11
573 in the supplementary), indicating that the AIS basal surface can be directly exposed to
574 these warm signals (warmer than the local freezing point temperature) with tide-like
575 oscillations (Figure 12). AM01 was located in the western flank of the AIS (Figure 1),
576 where the cold outflow rises buoyantly with frazil ice accreting to the ice base
577 (Herraiz-Borreguero et al., 2013). Our assessments showed that the tidal currents may be
578 significant in both the inflow and outflow beneath the AIS. We have not identified

579 similar tidal oscillations in the remaining thermosalinograph records, probably due to that
580 their depths were not sufficiently near the vertical fronts between two water masses,
581 which is necessary to accurately estimate tidal influences in temperature or salinity data.
582

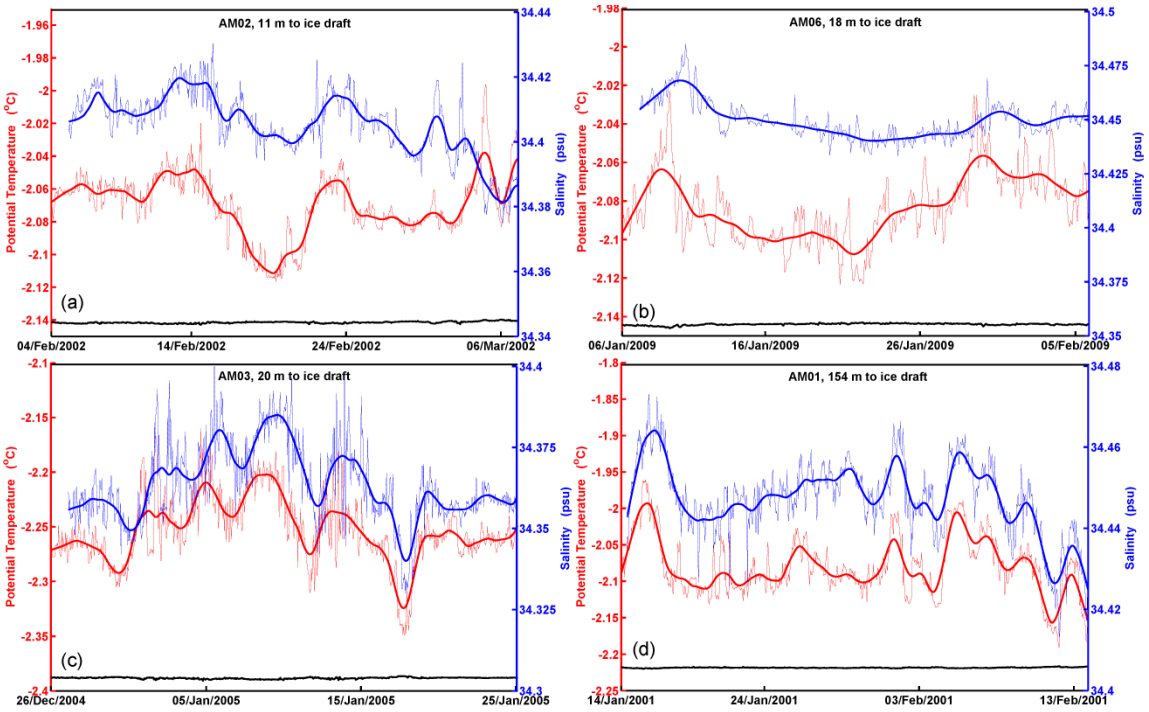

583

584 **Figure 12.** The first month of the temperature (thin red dashed lines; in °C) and
585 salinity (thin blue dashed lines; in psu) time series observed by thermosalinographs
586 deployed adjacent to the AIS basal surface the at the borehole sites of (a) AM02; (b)
587 AM06, (c) AM03 and (d) AM01 in the first month of the observational periods. The thick
588 red solid lines and the thick blue solid lines show the 2-day moving averages applied to
589 the original time series of temperature and salinity, respectively. The black line shows the
590 in situ freezing point temperature with respect to the in situ salinity and pressure, and
591 thereby ∇T is the difference between the observed potential temperature (red lines) and
592 the in situ freezing point (black lines).

593

In order to quantitatively clarify if the oscillations identified in the potential temperature and salinity records were related to tidal currents, we further assessed the power spectra of the potential temperature and salinity records from the 18 thermosalinographs deployed at the six borehole sites. As expected, only the observed potential temperature and salinity records shown in Figure 12 exhibited significant power spectra energy within the diurnal and semi-diurnal tidal frequency bands (Figure 13). In particular, the dominant peaks in the spectra fall at the M_2, O_1, K_1, and S_2 constituents at AM06 (Figure 13c-d). Note that the loggers of AM02, AM06, and AM03, which recorded significant tidal power spectra, were all deployed in the ocean layer adjacent to the AIS basal surface (Figure 2c), within the turbulent ice-ocean boundary layer (Jenkins et al., 2010; McPhee et al., 2008). As such, the tide-like pulsing of warm signals induced by the tidal currents in the ice shelf-ocean boundary layer may have direct influence on the AIS basal melting by modulating the turbulent heat flux at the ice-ocean interface (Hellmer & Olbers, 1989; Holland & Jenkins, 1999). The thermosalinographs deployed at a middle layer at AM01 also recorded the significant power spectra associated with the S_2, M_2, and O_1 tidal oscillations (Figure 13g-h). Since the buoyant ISW carrying enriched frazil ice ascended along the western flank of the AIS cavity (Craven et al., 2009; Herraiz-Borreguero et al., 2013), the power spectra peaks identified at AM01 implied that the tidal currents could have contributed to the transport and redistribution of frazil ice that promotes the AIS basal freezing rate (Galton-Fenzi et al., 2012). Therefore, these significant tide-like oscillations of potential temperature and salinity indicated that the

AIS basal mass balance can be significantly influenced by tidal currents and corresponding heat transport noted in sections 3.3 and 3.4.

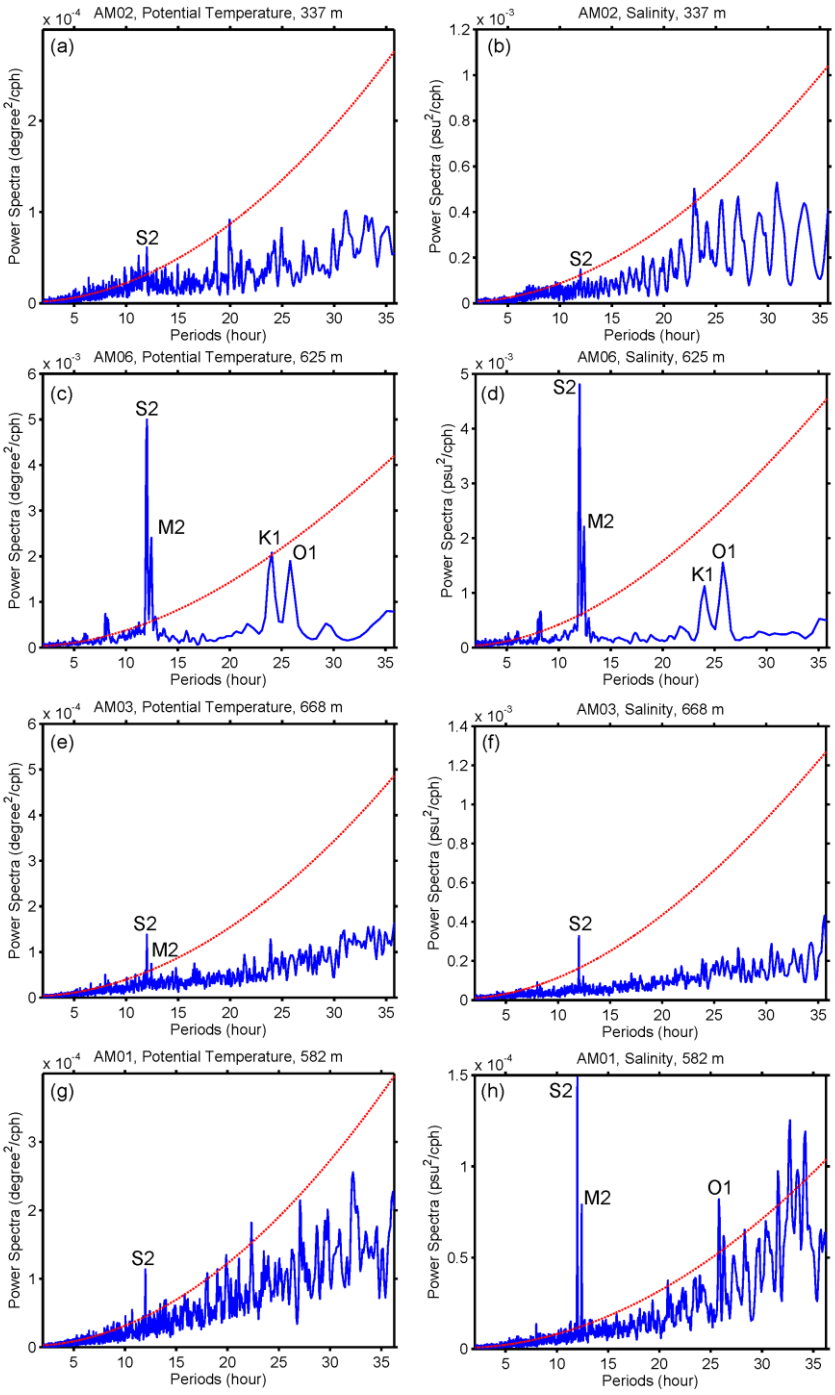

Figure 13. The power spectra (blue lines) of the potential temperature (a, c, e, g) and salinity (b, d, f, h) from the thermosalinographs equipped on the borehole sites for (a, b) AM02, (c, d) AM06, (e, f) AM03 and (g, h) AM01. The red dashed lines show the 95% confidence level.

4 Conclusions with Remarks

In this study, the tidal currents were quantitatively assessed based on 10 long-term moorings deployed over the continental shelf in Prydz Bay. By assessing the current meter records, in conjunction with the thermosalinograph records, we documented the characteristics of the tidal currents, the TKE, and the tidal heat transport. Tides in Prydz Bay were mixed diurnal-semidiurnal, and the observed tidal currents were much weaker than those in the Ross Sea and the Weddell Sea. As expected, the tidal energy was concentrated at the semidiurnal and diurnal tidal frequencies, with four main tidal constituents M_2, O_1, K_1, and S_2. Based on harmonic analysis for the observed currents, we found that the averaged magnitude of tidal currents was relatively larger in the Prydz Channel (3.3 cm s^{-1}) and decreased shoreward with the minimum (1.24 cm s^{-1}) occurring in the Svenner Channel. The major axes of the tidal ellipses were generally aligned south-north, steered by the topography, consistent with the results from previous observational and modeling studies (Nunes Vaz & Lennon, 1996; Padman et al., 2002; Hemer et al., 2006). Although the residual components of the current dominated the KE in Prydz Bay, the tidal contribution still cannot simply be neglected due to the indispensable proportion of TKE to KE, especially near the continental shelf break and at the AIS calving front. Considering the noticeable standard deviation of the heat transport induced by tidal currents, we confirmed the simulated tidal contribution to the heat content oscillation in the AIS cavity in Galton-Fenzi et al. (2012). Meanwhile, by assessing the rotary spectrum for all the current meter records, we also found that there is

644 a significant seasonality in the tidal currents. The tidal energy seems to be weakened in
645 the austral summer, yet the corresponding mechanism has not been clarified.

646 Based on the assessment of the hydrographic observations from the borehole sites
647 on the AIS, we found periodic oscillations of the potential temperature and salinity
648 records at the diurnal and semidiurnal tide frequency. In previous barotropic modeling
649 studies, the water column in the AIS cavity was believed to have strong stratification
650 induced by the melting of the AIS basal surface (Hemer et al., 2006; Maraldi et al., 2007).
651 These modeling studies argued that the simulated tidal mixing beneath the AIS is too
652 weak to overcome the stratification, and thereby the AIS basal surface was quite
653 inaccessible to the descending dense SW. Recently, both observational and modeling
654 studies revealed that warm mCDW can intrude onto the continental shelf and approach
655 the AIS calving front (Herraiz-Borreguero et al., 2016; Herraiz-Borreguero et al., 2015;
656 Liu et al., 2018; Williams et al., 2016), consistent with the mode 2 of ice shelf basal
657 melting pattern described in Jacobs et al. 1992 and Dinniman et al. 2016. The mCDW
658 intrusion in the AIS cavity was observed at the AM02 borehole site (70.33°E, 70.56°S),
659 indicating that the AIS cavity can be regarded as a partially warm cavity in autumn and
660 winter. Since the stratification between mCDW and ice shelf meltwater was not as strong
661 as that between dense SW and ice shelf meltwater, the warm mCDW may come into
662 contact with the AIS base without the requirement of strong vertical tidal mixing
663 identified in the Ross Ice Shelf and Filchner-Ronne Ice Shelf cavities. Meanwhile, the
664 tidal oscillations identified at AM01 may favor the transport and redistribution of frazil

ice. As such, we suggest that the tidal processes may act to influence the AIS basal mass balance even with relatively weak tidal currents.

Moreover, our quantitative assessment of the tidal currents in Prydz Bay is useful for further modeling studies, e.g., by providing constraints for open boundary conditions and validating the model results. Based on the observed tidal currents over the continental shelf, combined with the observed tide-like oscillations of the hydrographic characteristics in the AIS cavity, we argue that the tidal currents are expected to play an important role in regulating the AIS basal mass balance. The novel feature of this study is that it provides the benchmark validation for sensitivity experiments and open boundaries constraints in future modeling studies. However, due to the sparsity of observational data, the quantitative contribution of tides to the AIS basal mass balance and the mechanisms responsible for the tidal seasonality remain unexplored. Thus, it will be interesting to revisit the interactions between the AIS and the ocean in Prydz Bay by employing a coupled regional ocean-sea ice-ice shelf model that properly includes tidal processes.

Acknowledgments, Samples, and Data

This work is supported by the China National Natural Science Foundation (NSFC) Project (41941007; 41306208; 41876220; 41406214; 41376190; 41606217; 41606022), by the US National Science Foundation grants ANT-0739509 and PLR-1443444, by the Fundamental Research Funds for the Central Universities (2017B04814, 2017B20714), by Ocean Public Welfare Scientific Research Project(No. 201405031), by the Chinese Polar Environment Comprehensive Investigation & Assessment Program (CHINARE-2016-01-01), by the Natural Science Foundation of Jiangsu Province (BK20191405), by Program for Innovation Research and Entrepreneurship team in Jiangsu Province, and by a project funded by the Priority Academic Program Development of Jiangsu Higher Education Institutions (PAPD). Data from the 29th CHINARE are available through the Chinese National Arctic and Antarctic Data Center (http://www.chinare.org.cn/en/difDetailPublicDataset/?id=6725) and the National Oceanographic Data Center (ftp://ftp.nodc.noaa.gov/nodc/archive/arc0121/0173518/). The mooring data and borehole data from AMISOR are available through the Australian Antarctic Data Center (https://data.aad.gov.au/metadata/records/AMISOR_ship; https://data.aad.gov.au/metadata/records/ASAC_1164). The RTopo-2 data is available through the PANGAEA Data Publisher for Earth & Environmental Science (https://doi.pangaea.de/10.1594/PANGAEA.856844).

References

Castagno, P., Falco, P., Dinniman, M. S., Spezie, G., & Budillon, G. (2017). Temporal variability of the Circumpolar Deep Water inflow onto the Ross Sea continental shelf. *Journal of Marine Systems*, *166*, 37-49. https://doi.org/10.1016/j.jmarsys.2016.05.006

Cheng, C., Jenkins, A., Holland, P. R., Wang, Z., Liu, C., & Xia, R. (2019). Responses of sub-ice platelet layer thickening rate and frazil-ice concentration to variations in ice-shelf water supercooling in McMurdo Sound, Antarctica. *The Cryosphere*, *13*(1), 265-280. https://doi.org/10.5194/tc-13-265-2019

Cheng, C., Wang, Z., Liu, C., & Xia, R. (2017). Vertical Modification on Depth-Integrated Ice Shelf Water Plume Modeling Based on an Equilibrium Vertical Profile of Suspended Frazil Ice Concentration. *Journal of Physical Oceanography*, *47*(11), 2773-2792. https://doi.org/10.1175/jpo-d-17-0092.1

Craven, M., Allison, I., Brand, R., Elcheikh, A., Hunter, J., Hemer, M., & Donoghue, S. (2004). Initial borehole results from the Amery Ice Shelf hot-water drilling project. *Annals of Glaciology*, *39*, 531–539. https://doi.org/10.3189/172756404781814311

Craven, M., Allison, I., Fricker, H. A., & Warner, R. (2009). Properties of a marine ice layer under the Amery Ice Shelf, East Antarctica. *Journal of Glaciology*, *55*(192), 717-728. https://doi.org/10.3189/002214309789470941

722 Dinniman, M., Asay-Davis, X., Galton-Fenzi, B., Holland, P., Jenkins, A., &
723 Timmermann, R. (2016). Modeling Ice Shelf/Ocean Interaction in Antarctica: A
724 Review. *Oceanography*, *29*(4), 144-153. https://doi.org/10.5670/oceanog.2016.106
725 Fricker, H. A., Coleman, R., Padman, L., Scambos, T. A., Bohlander, J., & Brunt, K. M.
726 (2009). Mapping the grounding zone of the Amery Ice Shelf, East Antarctica using
727 InSAR, MODIS and ICESat. *Antarctic Science, 21*, 515–532.
728 https://doi.org/10.1017/S095410200999023X
729 Galton-Fenzi, B. K., Hunter, J. R., Coleman, R., Marsland, S. J., & Warner, R. C. (2012).
730 Modeling the basal melting and marine ice accretion of the Amery Ice Shelf. *Journal*
731 *of Geophysical Research: Oceans, 117*, C09031.
732 https://doi.org/10.1029/2012jc008214
733 Haigh, I. D., Pickering, M. D., Green, J. A. M., Arbic, B. K., Arns, A., Dangendorf, S., et
734 al. (2020). The Tides They Are A‐Changin': A Comprehensive Review of Past and
735 Future Nonastronomical Changes in Tides, Their Driving Mechanisms, and Future
736 Implications. *Reviews of Geophysics*, *58*(1). https://doi.org/10.1029/2018rg000636
737 Hellmer, H. H., & Olbers, D. J. (1989). A two-dimensional model for the thermohaline
738 circulation under an ice shelf. *Antarctic Science*, *1*(4), 325-336.
739 https://doi.org/10.1017/s0954102089000490
740 Hemer, M. A., Hunter, J. R., & Coleman, R. (2006). Barotropic tides beneath the Amery
741 Ice Shelf. *Journal of Geophysical Research, 111*, C11008.
742 https://doi.org/10.1029/2006jc003622

743 Herraiz-Borreguero, L., Allison, I., Craven, M., Nicholls, K. W., & Rosenberg, M. A.
744 (2013). Ice shelf/ocean interactions under the Amery Ice Shelf: Seasonal variability
745 and its effect on marine ice formation. *Journal of Geophysical Research: Oceans*,
746 *118*(12), 7117-7131. https://doi.org/10.1002/2013jc009158
747 Herraiz-Borreguero, L., Church, J. A., Allison, I., Peña-Molino, B., Coleman, R.,
748 Tomczak, M., & Craven, M. (2016). Basal melt, seasonal water mass transformation,
749 ocean current variability, and deep convection processes along the Amery Ice Shelf
750 calving front, East Antarctica. *Journal of Geophysical Research: Oceans*, *121*(7),
751 4946-4965. https://doi.org/10.1002/2016jc011858
752 Herraiz-Borreguero, L., Coleman, R., Allison, I., Rintoul, S. R., Craven, M., & Williams,
753 G. D. (2015). Circulation of modified Circumpolar Deep Water and basal melt
754 beneath the Amery Ice Shelf, East Antarctica. *Journal of Geophysical Research:*
755 *Oceans*, *120*(4), 3098-3112. https://doi.org/10.1002/2015jc010697
756 Holland, D. M., & Jenkins, A. (1999). Modeling Thermodynamic Ice-Ocean Interactions at
757 the Base of an Ice Shelf. *Journal of Physical Oceanography*, *29*(8), 1787-1800.
758 https://doi.org/10.1175/1520-0485(1999)0292.0.CO;2
759 Hulbe, C. L., Klinger, M., Masterson, M., Catania, G., Cruikshank, K., & Bugni, A.
760 (2016). Tidal bending and strand cracks at the Kamb Ice Stream grounding line,
761 West Antarctica. *Journal of Glaciology*, *62*(235), 816–824.
762 https://doi.org/10.1017/jog.2016.74

763 Jacobs, S. S., Helmer, H. H., Doake, C. S. M., Jenkins, A., & Frolich, R. M. (1992).
764 Melting of ice shelves and the mass balance of Antarctica. *Journal of Glaciology*,
765 *38*(130), 375-387.
766 Jendersie, S., Williams, M., Langhorne, P. J., & Robertson, R. (2018). The density-driven
767 winter intensification of the Ross Sea circulation. *Journal of Geophysical Research:*
768 *Oceans*, *123*, 7702–7724. https://doi.org/10.1029/2018JC013965
769 Jenkins, A., Nicholls, K. W., & Corr, H. F. J. (2010). Observation and Parameterization of
770 Ablation at the Base of Ronne Ice Shelf, Antarctica. *Journal of Physical*
771 *Oceanography*, *40*(10), 2298-2312. https://doi.org/10.1175/2010jpo4317.1
772 Johnson, E. S., & Van Woert, M. L. (2006). Tidal currents of the Ross Sea and their time
773 stability. *Antarctic Science*, 18(1), 141-154.
774 https://doi.org/10.1017/S0954102006000137
775 Jourdain, N. C., Molines, J.-M., Le Sommer, J., Mathiot, P., Chanut, J., de Lavergne, C., &
776 Madec, G. (2019). Simulating or prescribing the influence of tides on the Amundsen
777 Sea ice shelves. *Ocean Modelling*, *133*, 44-55.
778 https://doi.org/https://doi.org/10.1016/j.ocemod.2018.11.001
779 King, M. A., Coleman, R., & Morgan, P. (2000). Treatment of horizontal and vertical
780 tidal signals in GPS data: A case study on a floating ice shelf. *Earth, Planets and*
781 *Space*, *52*(11), 1043–1047. https://doi.org/10.1186/BF03352328

King, M., Colemar, R., & Nguyen, L. N. (2003). Spurious periodic horizontal signals in sub-daily GPS position estimates. *Journal of Geodesy*, *77*(1-2), 15-21. https://doi.org/10.1007/s00190-002-0308-z

Koentopp, M., Eisen, O., Kottmeier, C., Padman, L., & Lemke, P. (2005). Influence of tides on sea ice in the Weddell Sea: Investigations with a high-resolution dynamic-thermodynamic sea ice model. *Journal of Geophysical Research: Oceans*, *110*(C2). https://doi.org/10.1029/2004jc002405

Liu, C., Wang, Z., Cheng, C., Wu, Y., Xia, R., Li, B., & Li, X. (2018). On the Modified Circumpolar Deep Water Upwelling Over the Four Ladies Bank in Prydz Bay, East Antarctica. *Journal of Geophysical Research: Oceans*, *123*(11), 7819-7838. https://doi.org/10.1029/2018jc014026

MacAyeal, D. R. (1984). Thermohaline circulation below the Ross Ice Shelf: A consequence of tidally induced vertical mixing and basal melting. *Journal of Geophysical Research*, *89*(C1), 597. https://doi.org/10.1029/JC089iC01p00597

Makinson, K., & Nicholls, K. W. (1999). Modeling tidal currents beneath Filchner-Ronne Ice Shelf and on the adjacent continental shelf: their effect on mixing and transport. *Journal of Geophysical Research*, *104*(C6), 13449-13465.

Maraldi, C., Galton-Fenzi, B., Lyard, F., Testut, L., & Coleman, R. (2007). Barotropic tides of the Southern Indian Ocean and the Amery Ice Shelf cavity. *Geophysical Research Letters*, *34*(18). https://doi.org/10.1029/2007gl030900

802 McPhee, M. G., Morison, J. H., & Nilsen, F. (2008). Revisiting heat and salt exchange at
803 the ice-ocean interface: Ocean flux and modeling considerations. *Journal of*
804 *Geophysical Research*, *113*(C6). https://doi.org/10.1029/2007jc004383
805 Mellor, M., & McKinnon, G. (1960). The Amery Ice Shelf and its hinterland. *Polar*
806 *Record*, 10(64), 30–34. https://doi.org/10.1017/S0032247400050579
807 Müller, M., Cherniawsky, J., Foreman, M., & von Storch, J.-S. (2014). Seasonal variation
808 of the M2 tide, *Ocean Dynamics*, https://doi:10.1007/s10236-013-0679-0.
809 Mueller, R. D., Hattermann, T., Howard, S. L., Padman, L., Mueller, R. D., Hattermann,
810 T., et al. (2018). Tidal influences on a future evolution of the Filchner-Ronne Ice Shelf
811 cavity in the Weddell Sea, Antarctica. *The Cryosphere*, *12*(2), 453-476.
812 https://doi.org/10.5194/tc-12-453-2018
813 Murray, M. T. (1964). A General Method for the Analysis of Hourly Heights of Tide.
814 *International Hydrographic Review*, *41*(2), 91-101.
815 Nunes Vaz, R. A., & Lennon, G. W. (1996). Physical oceanography of the Prydz Bay
816 region of Antarctic waters. *Deep Sea Research Part I Oceanographic Research*
817 *Papers*, *43*(5), 603-641. https://doi.org/10.1016/0967-0637(96)00028-3
818 Ohshima, K. I., Fukamachi, Y., Williams, G. D., Nihashi, S., Roquet, F., Kitade, Y., et al.
819 (2013). Antarctic Bottom Water production by intense sea-ice formation in the Cape
820 Darnley polynya. *Nature Geoscience*, *6*, 235. Article.
821 https://doi.org/10.1038/ngeo1738

822 Ou, H.-W., Guan, X., & Chen, D. (2009). Tidal effect on the dense water discharge, Part 1:
823 Analytical model. *Deep Sea Research Part II: Topical Studies in Oceanography*,
824 *56*(13-14), 874-883. https://doi.org/10.1016/j.dsr2.2008.10.031
825 Padman, L., Erofeeva, S., & Joughin, I. A. N. (2003). Tides of the Ross Sea and Ross Ice
826 Shelf cavity. *Antarctic Science*, *15*(1), 31-40.
827 https://doi.org/10.1017/S0954102003001032
828 Padman, L., Erofeeva, S. Y., & Fricker, H. A. (2008). Improving Antarctic tide models by
829 assimilation of ICESat laser altimetry over ice shelves. *Geophysical Research Letters*,
830 *35*(22). https://doi.org/10.1029/2008gl035592
831 Padman, L., Fricker, H., Coleman, R., Howard, S., & Erofeeva, L. (2002). A new tide
832 model for the Antarctic Ice shelves and seas. *Annals of Glaciology*, *34*, 247-254.
833 https://doi.org/10.3189/172756402781817752
834 Padman, L., Howard, S., & Muench, R. (2006). Internal tide generation along the South
835 Scotia Ridge. *Deep-Sea Research Part II*, 53, 157–171.
836 https://doi.org/10.1016/j.dsr2.2005.07.011
837 Padman, L., Howard, S., Orsi, A., & Muench, R. (2009). Tides of the Northwestern Ross
838 Sea and their impact on dense outflows of Antarctic Bottom Water. *Deep Sea*
839 *Research Part II: Topical Studies in Oceanography*, *56*, 818-834.
840 https://doi.org/10.1016/j.dsr2.2008.10.026

841 Padman, L., Siegfried, M. R., & Fricker, H. A. (2018). Ocean Tide Influences on the
842 Antarctic and Greenland Ice Sheets. *Reviews of Geophysics*, *56*(1), 142-184.
843 https://doi.org/10.1002/2016rg000546
844 Pawlowicz, R., Beardsley, B., & Lentz, S. (2002). Classical tidal harmonic analysis
845 including error estimates in MATLAB using T_TIDE ☆. *Computers & Geosciences*,
846 *28*(8), 929-937. https://doi.org/10.1016/s0098-3004(02)00013-4
847 Pillsbury, R. D., & Jacobs, S. S. (1985). Preliminary Observations from Long-Term
848 Current Meter Moorings Near the Ross Ice Shelf, Antarctica. In *Oceanology of the*
849 *Antarctic Continental Shelf*, 87-107.
850 Ray, R. D., Loomis, B. D., Luthcke, S. B., & Rachlin, K. E. (2019). Tests of ocean-tide
851 models by analysis of satellite-to-satellite range measurements: an update.
852 *Geophysical Journal International*, *217*(2), 1174-1178.
853 https://doi.org/10.1093/gji/ggz062
854 Robinson, N. J. (2011). Circulation, mixing and interactions in the ocean near the Ross
855 Ice Shelf, Antarctica. PHD thesis, Univ. of Otago, Dunedin, New Zealand.
856 Robertson, R. (2001). Internal tides and baroclinicity in the Southern Weddell Sea: 2.
857 Effects of the critical latitude and stratification. *Journal of Geophysical Research:*
858 *Oceans*, *106*(C11), 27017-27034. https://doi.org/10.1029/2000jc000476
859 Robertson, R. (2013). Tidally induced increases in melting of Amundsen Sea ice shelves.
860 *Journal of Geophysical Research: Oceans*, *118*(6), 3138-3145.
861 https://doi.org/10.1002/jgrc.20236

Robertson, R. (2016). Outflow from under the Pine Island Bay Ice Shelf: Fine Scale Structure and its Temporal Variability. *Advances in Polar Science*, *27*, 245-263. https://doi.org/10.13679/j.advps.2016.4.00245

Robertson, R., Padman, L., & Egbert, G. D. (1998). Tides in the Weddell Sea. In *Ocean, Ice, and Atmosphere: Interactions at the Antarctic Continental Margin* (pp. 341-369).

Schaffer, J., Timmermann, R., Arndt, J. E., Kristensen, S. S., Mayer, C., Morlighem, M., & Steinhage, D. (2016). A global, high-resolution data set of ice sheet topography, cavity geometry, and ocean bathymetry. *Earth System Science Data*, *8*(2), 543-557. https://doi.org/10.5194/essd-8-543-2016

Semper, S., & Darelius, E. (2017). Seasonal resonance of diurnal coastal trapped waves in the southern Weddell Sea, Antarctica. *Ocean Sci.*, *13*(1), 77-93. https://doi.org/10.5194/os-13-77-2017

St-Laurent P., Saucier, F. J., & Dumais, J. F. (2008). On the modification of tides in a seasonally ice-covered sea. J. Geophys. Res. 113. https://doi.org/10.1029/2007JC004614

St-Laurent, P., Klinck, J. M., & Dinniman, M. S. (2013). On the Role of Coastal Troughs in the Circulation of Warm Circumpolar Deep Water on Antarctic Shelves. *Journal of Physical Oceanography*, *43*(1), 51-64. https://doi.org/10.1175/jpo-d-11-0237.1

Stewart, A. L., Klocker, A., & Menemenlis, D. (2018). Circum-Antarctic Shoreward Heat Transport Derived From an Eddy- and Tide-Resolving Simulation. *Geophysical Research Letters*, *45*(2), 834-845. https://doi.org/10.1002/2017gl075677

883 Wang, Q., Danilov, S., Hellmer, H., Sidorenko, D., Schröter, J., & Jung, T. (2013).
884 Enhanced cross-shelf exchange by tides in the western Ross Sea. *Geophysical*
885 *Research Letters*, *40*(21), 5735-5739. https://doi.org/10.1002/2013gl058207
886 Wang, Q., Danilov, S., Hellmer, H. H., & Schröter, J. (2010). Overflow dynamics and
887 bottom water formation in the western Ross Sea: Influence of tides. *Journal of*
888 *Geophysical Research: Oceans*, *115*(C10). https://doi.org/10.1029/2010jc006189
889 Whitworth, T., & Orsi, A. H. (2006). Antarctic Bottom Water production and export by
890 tides in the Ross Sea. *Geophysical Research Letters*, *33*(12).
891 https://doi.org/10.1029/2006gl026357
892 Williams, G. D., Herraiz-Borreguero, L., Roquet, F., Tamura, T., Ohshima, K. I.,
893 Fukamachi, Y., et al. (2016). The suppression of Antarctic bottom water formation by
894 melting ice shelves in Prydz Bay. *Nat Commun*, *7*(1).
895 https://doi.org/10.1038/ncomms12577